

UC Santa Cruz

UC Santa Cruz Electronic Theses and Dissertations

Title

Nanostructured Hematite for Photoelectrochemical Water Splitting

Permalink

<https://escholarship.org/uc/item/5p46g2kn>

Author

Ling, Yichuan

Publication Date

2014

Peer reviewed|Thesis/dissertation

UNIVERSITY OF CALIFORNIA
SANTA CRUZ

Nanostructured Hematite for Photoelectrochemical Water Splitting

Dissertation submitted in partial satisfaction
of the requirements for the degree of

DOCTOR OF PHILOSOPHY

in

CHEMISTRY

by

Yichuan Ling

June 2014

The Dissertation of Yichuan Ling is
approved:

Professor Yat Li, chair

Professor Jin Z. Zhang

Professor Scott R. J. Oliver

Tyrus Miller
Vice Provost and Dean of Graduate Studies

Copyright © by
Yichuan Ling
2014

Table of Contents

List of Figures	v
Abstract	vii
Dedication	ix
Acknowledgements	x
Chapter 1	1
Introduction of Hematite Nanostructures for Photoelectrochemical Water Splitting	1
Abstract	1
Introduction	2
1.1 The Principle of Photoelectrochemical Water Splitting	3
1.2 Advances of Using Hematite as Photoanode	4
1.3 Element-doped Nanostructured Hematite Photoanode	5
1.4 Oxygen-deficient Hematite Photoanode	6
1.5 PEC Performance Measurement	7
References	8
Chapter 2	17
Sn-doped Hematite Nanostructures for Photoelectrochemical Water Splitting	17
Abstract	17
2.1 Introduction	18
2.2 Experimental Section	20
2.3 Results and Discussion	23
2.4 Conclusion	43
References	44
Chapter 3	49
The Influence of Oxygen Content on Thermal Activation of Hematite Nanowires	49
Abstract	49

3.1 Introduction.....	50
3.2 Experimental section:.....	51
3.3 Results and Discussion	54
3.4 Conclusion	67
References.....	68
Chapter 4.....	72
Low Temperature Activation of Hematite Nanowires for Photoelectrochemical Water Oxidation	72
Abstract.....	72
4.1 Introduction.....	73
4.2 Experimental Section	75
4.3 Results and Discussion	78
4.4 Conclusion	91
References.....	92
Chapter 5.....	97
Final Conclusions and Outlook.....	97
5.1 Final conclusions of the thesis	97
5.2 Outlook	100
References.....	102
Bibliography	104

List of Figures

Chapter 1

Figure 1.1 Schematic of photoelectrochemical cell.

Figure 1.2 Scheme of three-electrode PEC cell and PEC measurement system.

Chapter 2

Figure 2.1 SEM images and XRD patterns of hematite nanowires

Figure 2.2 XPS spectra of hematite nanowires and nanocorals

Figure 2.3 Linear sweeps and IPCE curves of hematite nanowires

Figure 2.4 SEM images of hematite nanocorals

Figure 2.5 SEM images and XRD patterns of hematite nanostructures

Figure 2.6 Linear sweeps and IPCE curves of Sn-doped hematite nanocorals

Figure 2.7 Mott-Schottky plots of hematite nanowires and Sn-doped nanocorals

Figure 2.8 Ultrafast transient absorption decay profiles of hematite nanowires

Chapter 3

Figure 3.1 SEM images of FeOOH and hematite nanowire arrays

Figure 3.2 XRD spectra of FeOOH and hematite nanowire arrays

Figure 3.3 Linear sweeps of N- and A-hematite photoanodes

Figure 3.4 IPCE of N- and A-hematite photoanodes

Figure 3.5 Mott-Schottky curves of N- and A-hematite photoanodes

Figure 3.6 Fe 2P XPS spectra of N- and A-hematite samples

Figure 3.7 Digital photos of FeOOH and hematite nanowires prepared under different sintering environments

Figure 3.8 Raman and XRD spectra of hematite nanowires

Chapter 4

Figure 4.1 Schematic illustration, digital photos, and SEM photos of β -FeOOH and its thermal decomposition products at different temperatures

Figure 4.2 XRD spectra of β -FeOOH and its thermal decomposition products

Figure 4.3 Raman spectra of β -FeOOH and its thermal decomposition products

Figure 4.4 Schematic illustration, XRD and Raman spectra of thermal re-oxidation of magnetite to hematite samples

Figure 4.5 XPS spectra of hematite samples

Figure 4.6 Nyquist plots of the impedance of hematite photoanodes

Figure 4.7 Linear sweeps of hematite photoanodes

Figure 4.8 IPCE spectra of hematite photoanodes

Figure 4.9 Linear sweeps of Sn-doped hematite photoanodes

Figure 4.10 IPCE spectra of Sn-doped hematite photoanodes

Figure 4.11 Nyquist plots of Sn-doped hematite photoanodes

Figure 4.12 Amperometric i-t curves of hematite photoanodes

Abstract

Nanostructured Hematite for Photoelectrochemical Hydrogen Generation

By

Yichuan Ling

Solar water splitting is an environmentally friendly reaction of producing hydrogen gas. Since Honda and Fujishima first demonstrated solar water splitting in 1972 by using semiconductor titanium dioxide (TiO_2) as photoanode in a photoelectrochemical (PEC) cell, extensive efforts have been invested into improving the solar-to-hydrogen (STH) conversion efficiency and lower the production cost of photoelectrochemical devices. In the last few years, hematite ($\alpha\text{-Fe}_2\text{O}_3$) nanostructures have been extensively studied as photoanodes for PEC water splitting. Although nanostructured hematite can improve its photoelectrochemical water splitting performance to some extent, by increasing active sites for water oxidation and shortening photogenerated hole path length to semiconductor/electrolyte interface, the photoactivity of pristine hematite nanostructures is still limited by a number of factors, such as poor electrical conductivities and slow oxygen evolution reaction kinetics. Previous studies have shown that tin (Sn) as an *n*-type dopant can substantially enhance the photoactivity of hematite photoanodes by modifying their optical and electrical properties. In this thesis, I will first demonstrate an unintentional Sn-doping method via high temperature annealing of hematite nanowires grown on

fluorine-doped tin oxide (FTO) substrate to enhance the donor density. In addition to introducing extrinsic dopants into semiconductors, the carrier densities of hematite can also be enhanced by creating intrinsic defects. Oxygen vacancies function as shallow donors for a number of hematite. In this regard, I have investigated the influence of oxygen content on thermal decomposition of FeOOH to induce oxygen vacancies in hematite. In the end, I have studied low temperature activation of hematite nanostructures.

Dedication

**DEDICATED
TO
XUNYE LING, JING LI, YIFENG LING**

Acknowledgements

In my five-year PhD study, I've learnt a lot from my advisor and all my lab colleagues. Research is like a long journey, now it's time to have a short break, review the unforgettable moments, and outlook the future. I will keep the enthusiasm to explore the unknown, and continue to work hard in the future. I would like to take this opportunity to express my sincere thanks to the people around me.

First of all, I want to express my thanks to my advisor, Prof. Yat Li, for his inspiring guidance and continuous support. More importantly, I have learnt a lot of things from him, not only the research methods and logics, but also the attitude for life. He keeps asking me what the key points are and what the novelty of the current work is. At the beginning, it is really hard for me to answer these questions. However, it is indeed a good training for me to be a good researcher. Now, I am always thinking these questions when I start a new project. Besides, he always encourages me to be more confident, especially during the presentation during the conferences and interviews. I will keep these advices in my mind. I would also like to thank Prof. Li's wife, Fang Qian, for her nice help and discussion in both my research and my life. I feel I am so lucky to join this group.

Secondly, I would like to thank my oral and thesis committee, Prof. Jin Z. Zhang, Prof. and Scott R. J. Oliver, and Prof. Sue Carter as the outside member in my Oral Qualifying Examination. They always hold a high standard for each student and try their best to make the start of their career a success. Especially, I want to thank Prof. Jin Z. Zhang. We have collaborations of several projects using femtosecond layer system to study the ultrafast dynamics in nanostructure semiconductors. I have learnt a lot from his inspiring suggestions during each discussion.

Thirdly, I would like to thank Yat's first student, Dr. Gongming Wang. He is my teacher, my exemplar, and my best friend. I really appreciate all the helps he gave to me not only in research but also in life when I came to UC Santa Cruz. Besides, I would say thank you to my roommates, Hanyu Wang and Yang Song. They've create a warm home in 606 Koshland Way, which is very precious for student abroad like me. I will not forget those days living there. I would also like to thank all the former and current members in Li lab, including, Dr. Xunyu Yang, Dr. Xihong Lu, Feng Luan, Prof. Dingshen Yuan, Prof. Xiaoxia Liu, Dr. Ying-Chih Pu, Yi Yang, Tianyu Liu and Teng Zhai for their helps in my research projects. I also want to express my thanks to my friends in Shaowei's lab, including Dr. Xiongwu Kang, Ke Liu, Peiguang Hu, Limei Chen; friends in Jin's lab, including Dr. Jason K. Cooper, Dr. Damon A. Wheeler,

Shraz Gul, Dr. Bob Fitzmorris, Staci Adams, Sarah Lindley, and Liat Zavodivker.

Finally, I really need thank my father, Xunye Ling, my mother, Jing Li, and my twin brother, Yifeng Ling. Without your support and understanding, I cannot come to UC Santa Cruz and finish my PhD studies. I know my parents always hold a great hope for me and I will not let them down. I also want to express my thanks to my girlfriend, Ynes Peng. Without your understanding and support, I cannot be here. I cherish everything you have done for me in my heart, and I love you.

The text of this dissertation includes reprints of the following previously published or subsequently published materials.

1. “Sn-doped hematite nanostructures for photoelectrochemical water splitting”
Ling Y., Wang G., Wheeler D. A., Zhang J. Z. and Li Y., *Nano Lett.* **2011**, 11, 2119-2125.
2. “Influence of oxygen content on thermal activation of hematite nanowires”
Ling Y., Wang G., Reddy J., Wang C. C., Zhang J. Z. and Li Y., *Angew. Chem. Int. Ed.* **2012**, 51, 4074-4079.
3. “Optical properties, and application of hematite (α -Fe₂O₃) nanostructures”

Ling Y., Wheeler D. A., Zhang J. Z., and Li Y., book chapter for *One-Dimensional Nanostructures: Principles and Applications*, edited by J. Yao and T. Zhai, John Wiley & Sons, Inc. Hoboken, New Jersey, **2013**.

4. “Low temperature activation of hematite nanowires for photoelectrochemical water oxidation” **Ling Y.**, Wang G., Wang H., Yang Y., and Yat Li., *ChemSusChem*. **2014**, 7, 848-853.

Chapter 1

Introduction of Hematite Nanostructures for Photoelectrochemical Water Splitting

Abstract

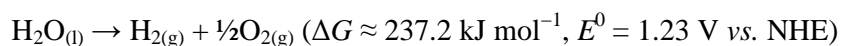
Seeking renewable and sustainable energy sources becomes urgent problem recently due to the rapid increase demand for energy with the ever-growing of global population. Photoelectrochemical (PEC) water splitting is a promising environmentally benign method for direct solar energy conversion to storable fuels such as hydrogen (H_2), offering an attractive way toward less reliance on fossil fuels. Hematite ($\alpha\text{-Fe}_2\text{O}_3$) nanostructures have been extensively studied as photoanodes for PEC water splitting. However, the photoactivity of pristine hematite nanostructures is limited by a number of factors, such as poor electrical conductivities and slow oxygen evolution reaction kinetics. Previous studies have shown that tin (Sn) as an *n*-type dopant can substantially enhance the photoactivity of hematite photoanodes by modifying their optical and electrical properties. In the part, I will give an overview of the basic mechanism of photoelectrochemical water splitting, advances in using element-doped and oxygen-deficient nanostructured hematite photoanodes, and PEC performance measurements.

Introduction

The ever-growing of global population and the standard of living has resulted in a steadily increased energy demanding. Today, the energy crisis is becoming one of the most urgent issues in human being's society. Because of this, seeking renewable and sustainable energy sources is believed a potential solution to solve the faced energy crisis of our time. Among many varieties of sustainable energy sources (such as solar, wind, hydropower, and geothermal), efficient conversion of solar energy into useful forms has attracted a lot of attentions due to the huge amount of energy available. Every year, the total solar energy flux reaching the Earth's surface is about 125,000 TW.¹ The successful harvesting of 0.04% of the solar energy can produce 50 TW of energy, which is sufficient to cover global energy needs. One of the most attractive means proposed to fully utilize solar energy is to convert solar energy into electrical energy or provide access to chemical energy stored in fuels such as hydrogen. Hydrogen is potentially high-efficiency fuel with high energy density of ~140 MJ/Kg.¹ Besides, hydrogen is a chemical fuel that can react with oxygen in a hydrogen fuel cell to produce electricity, with water as a side product. Therefore, production of hydrogen in an environment-friendly and effective way is highly desirable.

1.1 The Principle of Photoelectrochemical Water Splitting

Solar water splitting is an environmentally friendly reaction of producing hydrogen gas,¹⁻⁹ which is known to be an endothermic process:



This process can be achieved in a PEC cell using n-type semiconductor as the photoanode in the presence of a metal cathode (**Figure 1a**). For candidate n-type semiconductor for photoanode like metal oxides, only large bandgap metal oxides such as anatase TiO_2 , SrTiO_3 and KTaO_3 can straddle the water reduction and oxidation potentials.⁸ However, due to their bandgaps, only small amount of sunlight, especially in the UV region can be absorbed and used. This limitation combined with the overpotential and ohmic drop losses restrict the energy conversion performance of PEC cell. To solve this problem, extensive efforts have been invested into improving the solar-to-hydrogen (STH) conversion efficiency and lower the production cost of photoelectrochemical devices. The “Z-scheme” photoelectrochemical device consisting of a photoanode and a photocathode has been demonstrated to be a promising approach to achieve direct water splitting⁹⁻¹³ (**Figure 1b**). In this device, photoexcited electrons in photocathode will diffuse to semiconductor/electrolyte interface to generate hydrogen, while photo-generated holes in photoanode will be used in water oxidation. In such a Z-scheme device, the photocurrents of photocathode and photoanode have to be matched in order to get the optimal performance. In the last few years, researchers have made significant progress in developing high performance photocathodes. For example, it has been reported

that Rh-modified single-crystal InP has achieved STH efficiency of 13%.^{14, 15} Besides, planar Pt/n⁺p-Si photocathodes show about 30 mA/cm² photocurrent under one sun, which is close to 10% STH conversion efficiency¹⁶. On the other hand, photoanodes still have lower photocurrent density, which limits the overall efficiency for direct water splitting⁹⁻¹¹.

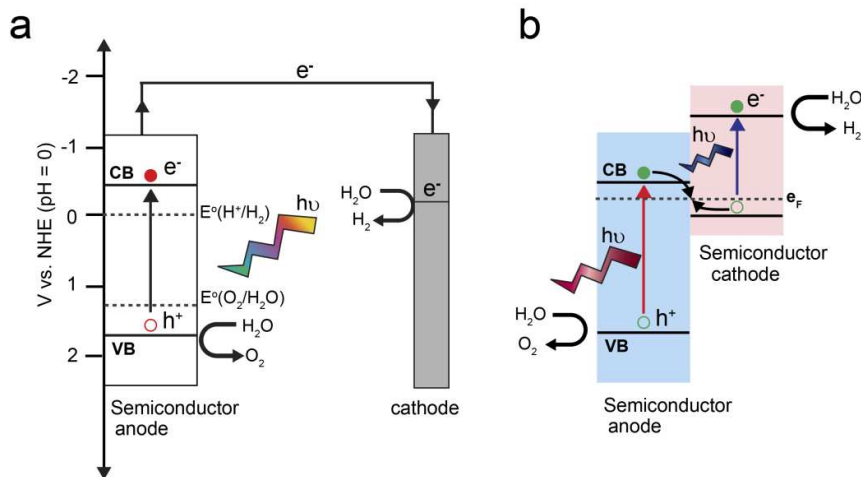


Figure 1.1 (a) Scheme of photoelectrochemical water splitting cell based on *n*-type semiconductor photoanode. VB and CB are the abbreviations for valence band and conduction band, respectively. (b) Schematic illustration of a Z-scheme photoelectrochemical device. Solid and empty circles represent photoexcited electrons and holes.

1.2 Advances of Using Hematite as Photoanode

A number of *n*-type semiconductors, such as TiO₂,^{7, 17-26} ZnO,²⁷⁻³⁴ WO₃,³⁵⁻⁴¹ and BiVO₄,^{13, 37, 42-53} have been studied as photoanode materials for water splitting. Among them, hematite is one of the most attractive materials for photoanode.^{1, 2, 54-58} Hematite has a favorable optical bandgap around 1.9-2.2 eV⁵⁹ for harvesting solar light, which corresponding to a high theoretical STH conversion efficiency of 14-17%.⁶⁰ Iron is the fourth most abundant element in

the Earth's crust (6.3% by weight)⁵ and hematite is a low cost material. In addition, hematite is chemically stable in solutions of different pH.⁶¹ However, the STH conversion efficiencies of reported hematite photoanodes are considerably lower than the theoretical value, owing to its very short excited state lifetime (<10 ps),⁶² short hole diffusion length (~2-4 nm),^{5,61} poor surface oxygen evolution reaction kinetics,⁶³ and poor electrical conductivity ($10^{-6} \Omega^{-1} \text{cm}^{-1}$).⁵

1.3 Element-doped Nanostructured Hematite Photoanode

The recent development of hematite nanostructures, including nanoparticles,^{59, 64, 65} nanowires,^{66, 67} and nanonets,^{56, 58} opens up new opportunities in addressing the abovementioned limitations. Nanostructured photoanode offers increased semiconductor/electrolyte interfacial area for water oxidation, as well as substantially reduced diffusion length for minority carriers. Therefore, nanostructured hematite photoelectrodes are expected to be more efficient in charge carrier collection than their bulk counterparts.⁶⁰ For example, Lin *et al.* reported the growth of ultrathin hematite film (25 nm) on a conductive nanonet structure. The nanonet-based hematite photoanode achieved an excellent photocurrent of 1.6 mA/cm^2 at 1.23 V *vs.* RHE, which is four times higher than the value obtained from the planar sample with the same thickness. The photocurrent enhancement was due to the increased activation sites for water oxidation.⁵⁶

The recent development of nanostructured hematite electrodes improved

their performance by increasing the effective surface area and decreasing the diffusion length for minority carriers, however it does not improve the intrinsic optical and electronic properties of the electrode materials. To further improve the photoactivity of hematite photoanode, element doping has been extensively studied to improve the structural, electronic and optical properties of hematite. The role of dopants, such as Ti,^{65, 68-75} Si,^{68, 76-79} Al,^{71, 80} Mg,^{81, 82} Zn,^{71, 78} Be,⁸⁰ Mo,⁸³ and Sn,^{4, 61, 69, 80, 81, 84-90} on the PEC performance of hematite have been investigated. Recently, there is an increasing interest of developing Sn-doped hematite nanostructured photoanode due to the significant effect of Sn doping on the photoactivity of hematite. Sn⁴⁺ is a tetravalent dopant that can be substitutionally doped into hematite at the Fe³⁺ sites.^{69, 71, 89} The electrical conductivity of Sn-doped hematite is enhanced by the occurrence of bivalent ions, Fe²⁺. The local pairs of Fe²⁺-Sn⁴⁺ play a role as donor centers in the hematite, causing enhanced electroconductivity.⁸⁴

1.4 Oxygen-deficient Hematite Photoanode

Although elemental doping has been proved to be effective in manipulating the properties of hematite, the incorporation of dopants could be challenging, due to the size discrepancy between the dopant atom and the element of host crystal, especially for large sized metal atoms. In addition to introducing extrinsic dopants into semiconductors, the carrier densities of metal oxide can also be enhanced by creating intrinsic defects. Oxygen vacancies function as shallow donors for a number of metal oxides, including hematite.^{18, 55} Several approaches can be used to introduce oxygen vacancies. For example, Wang and

co-workers in our lab have demonstrated that oxygen vacancies can be created in TiO_2 by a simple hydrogenation process.¹⁸ Samples with oxygen vacancies yield substantially enhanced photocurrent densities. We anticipated that creating oxygen vacancy (V_o) and thereby Fe^{2+} sites in hematite could significantly increase its conductivity via a polaron hopping mechanism.⁵⁵ However, the same hydrogenation method is not appropriate for hematite because it is more easily to be reduced in hydrogen to photo-inactive black magnetite, which shows no photocurrent. Alternatively, we prepared highly conductive and photoactive hematite through thermal decomposition of $\beta\text{-FeOOH}$ in an oxygen-deficient atmosphere ($\text{N}_2 + \text{air}$). The oxygen content during thermal activation affects significantly the formation of V_o and thereby the photoactivity of hematite nanowires for water oxidation. This is the first demonstration of highly photoactive hematite nanowire arrays at relatively low activation temperature without element dopant.

1.5 PEC Performance Measurement

A three-electrode PEC cell was used to measure the PEC performance of the hematite photoanodes (Figure 1.2a) Hematite nanostructure samples were the working electrodes. A coiled Pt wire was used as a counter electrode and an Ag/AgCl (1M KCl) electrode was used as a reference electrode. The Electrolyte was 1M NaOH aqueous solution (pH 13.6), deaerated by purging N_2 gas into electrolyte. The PEC measurements were recorded by an electrochemical workstation (Model CHI 660D, CH instruments, Inc., Austin, TX); and a solar simulator (Newport, Model 69907) coupled to a filter (AM 1.5G) using a 150 W

Xenon lamp as the white light source (Figure 1.2b).

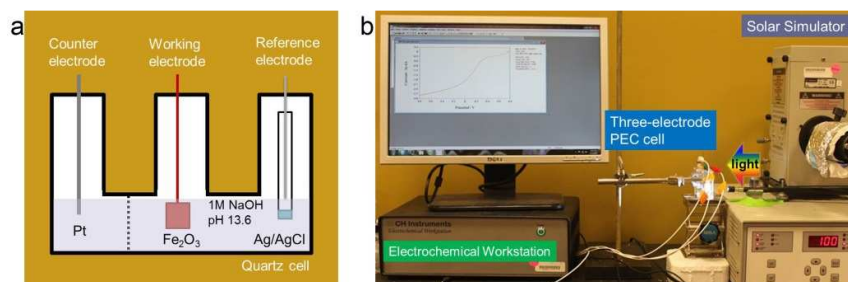


Figure 1.2 (a) Scheme of three-electrode PEC cell. (b) Schematic illustration of PEC measurement system.

References

1. Li, Y.; Zhang, J. Z. *Laser & Photonics Reviews* **2010**, 4, (4), 517-528.
2. Wheeler, D. A.; Wang, G.; Ling, Y.; Li, Y.; Zhang, J. Z. *Energy Environ. Sci.* **2012**, 5, (5), 6682-6702.
3. Gratzel, M. *Nature* **2001**, 414, (6861), 338-344.
4. Sivula, K.; Zboril, R.; Le Formal, F.; Robert, R.; Weidenkaff, A.; Tucek, J.; Frydrych, J.; Gratzel, M. *J Am Chem Soc* **2010**, 132, (21), 7436-7444.
5. Sivula, K.; Le Formal, F.; Grätzel, M. *ChemSusChem* **2011**, 4, (4), 432-449.
6. Wang, G.; Ling, Y.; Li, Y. *Nanoscale* **2012**, 4, (21), 6682-6691.
7. Fujishima, A.; Honda, K. *Nature* **1972**, 238, (5358), 37-+.
8. Bak, T.; Nowotny, J.; Rekas, M.; Sorrell, C. C. *Int J Hydrogen Energ* **2002**, 27, (10), 991-1022.
9. Wang, G.; Ling, Y.; Wang, H.; Xihong, L.; Li, Y. *Journal of Photochemistry and Photobiology C: Photochemistry Reviews* **2014**, 19, (0), 35-51.

10. Coridan, R. H.; Shaner, M.; Wiggernhorn, C.; Brunshwig, B. S.; Lewis, N. S. *The Journal of Physical Chemistry C* **2013**, 117, (14), 6949-6957.
11. Liu, C.; Tang, J.; Chen, H. M.; Liu, B.; Yang, P. *Nano Lett* **2013**, 13, (6), 2989-2992.
12. Warren, E. L.; Boettcher, S. W.; McKone, J. R.; Lewis, N. S. In *Photoelectrochemical water splitting: silicon photocathodes for hydrogen evolution*, 2010; 2010; pp 77701F-77701F-7.
13. Park, H. S.; Lee, H. C.; Leonard, K. C.; Liu, G.; Bard, A. J. *Chemphyschem* **2013**, 14, (10), 2277-2287.
14. Heller, A. *Science* **1984**, 223, (4641), 1141-1148.
15. Aharon-Shalom, E.; Heller, A. *J Electrochem Soc* **1982**, 129, (12), 2865-2866.
16. Boettcher, S. W.; Warren, E. L.; Putnam, M. C.; Santori, E. A.; Turner-Evans, D.; Kelzenberg, M. D.; Walter, M. G.; McKone, J. R.; Brunshwig, B. S.; Atwater, H. A.; Lewis, N. S. *J Am Chem Soc* **2011**, 133, (5), 1216-1219.
17. Hensel, J.; Wang, G.; Li, Y.; Zhang, J. Z. *Nano Lett.* **2010**, 10, 478-483.
18. Wang, G.; Wang, H.; Ling, Y.; Tang, Y.; Yang, X.; Fitzmorris, R. C.; Wang, C.; Zhang, J. Z.; Li, Y. *Nano Lett* **2011**, 11, (7), 3026-3033.
19. Wang, H.; Wang, G.; Ling, Y.; Lepert, M.; Wang, C.; Zhang, J. Z.; Li, Y. *Nanoscale* **2012**, 4, (5), 1463-1466.

20. Hwang, Y. J.; Hahn, C.; Liu, B.; Yang, P. *ACS Nano* **2012**, 6, (6), 5060-5069.
21. Hoang, S.; Guo, S.; Hahn, N. T.; Bard, A. J.; Mullins, C. B. *Nano Lett* **2012**, 12, (1), 26-32.
22. Hoang, S.; Berglund, S. P.; Hahn, N. T.; Bard, A. J.; Mullins, C. B. *J Am Chem Soc* **2012**, 134, (8), 3659-3662.
23. Xu, M.; Da, P.; Wu, H.; Zhao, D.; Zheng, G. *Nano Lett* **2012**, 12, (3), 1503-1508.
24. DeSario, P. A.; Pietron, J. J.; DeVantier, D. E.; Brintlinger, T. H.; Stroud, R. M.; Rolison, D. R. *Nanoscale* **2013**, 5, (17), 8073-8083.
25. Ni, M.; Leung, M. K. H.; Leung, D. Y. C.; Sumathy, K. *Renewable and Sustainable Energy Reviews* **2007**, 11, (3), 401-425.
26. Zhen, C.; Wang, L.; Liu, L.; Liu, G.; Lu, G. Q.; Cheng, H.-M. *Chem. Commun. (Camb.)* **2013**, 49, (55), 6191-6193.
27. Pu, Y.-C.; Wang, G.; Chang, K.-D.; Ling, Y.; Lin, Y.-K.; Fitzmorris, B. C.; Liu, C.-M.; Lu, X.; Tong, Y.; Zhang, J. Z.; Hsu, Y.-J.; Li, Y. *Nano Lett* **2013**, 13, (8), 3817-3823.
28. Cooper, J. K.; Ling, Y.; Longo, C.; Li, Y.; Zhang, J. Z. *The Journal of Physical Chemistry C* **2012**, 116, (33), 17360-17368.
29. Yang, X. Y.; Wolcott, A.; Wang, G. M.; Sobo, A.; Fitzmorris, R. C.; Qian, F.; Zhang, J. Z.; Li, Y. *Nano Lett* **2009**, 9, (6), 2331-2336.

30. Wang, G. M.; Yang, X. Y.; Qian, F.; Zhang, J. Z.; Li, Y. *Nano Lett* **2010**, 10, (3), 1088-1092.
31. Xie, S.; Lu, X.; Tong, Y. In *An effective way to enhance photoelectrochemical photoactivity and stability of ZnO nanorod arrays by carbon and nitrogen co-treatment*, International Photonics and Optoelectronics Meetings (POEM), Wuhan, 2013; Optical Society of America: Wuhan, 2013; p ASa3A.28.
32. Shi, J.; Starr, M. B.; Xiang, H.; Hara, Y.; Anderson, M. A.; Seo, J.-H.; Ma, Z.; Wang, X. *Nano Lett* **2011**, 11, (12), 5587-5593.
33. Xie, S.; Lu, X.; Zhai, T.; Li, W.; Yu, M.; Liang, C.; Tong, Y. *J Mater Chem* **2012**, 22, (28), 14272-14275.
34. Lin, Y.-G.; Hsu, Y.-K.; Chen, Y.-C.; Chen, L.-C.; Chen, S.-Y.; Chen, K.-H. *Nanoscale* **2012**, 4, (20), 6515-6519.
35. Su, J. Z.; Guo, L. J.; Bao, N. Z.; Grimes, C. A. *Nano Lett* **2011**, 11, (5), 1928-1933.
36. Wang, G.; Ling, Y.; Wang, H.; Yang, X.; Wang, C.; Zhang, J. Z.; Li, Y. *Energy Environ. Sci.* **2012**, 5, (3), 6180-6187.
37. Zhang, X.; Lu, X.; Shen, Y.; Han, J.; Yuan, L.; Gong, L.; Xu, Z.; Bai, X.; Wei, M.; Tong, Y.; Gao, Y.; Chen, J.; Zhou, J.; Wang, Z. L. *Chem. Commun. (Camb.)* **2011**, 47, (20), 5804-5806.
38. Jin, T.; Diao, P.; Wu, Q.; Xu, D.; Hu, D.; Xie, Y.; Zhang, M. *Applied*

Catalysis B: Environmental **2014**, 148-149, 304-310.

39. Cristino, V.; Caramori, S.; Argazzi, R.; Meda, L.; Marra, G. L.; Bignozzi, C.
A. Langmuir **2011**, 27, (11), 7276-7284.
40. Esposito, D. V.; Forest, R. V.; Chang, Y.; Gaillard, N.; McCandless, B. E.;
Hou, S.; Lee, K. H.; Birkmire, R. W.; Chen, J. G. *Energy Environ. Sci.*
2012, 5, (10), 9091-9099.
41. Kronawitter, C. X.; Vayssieres, L.; Shen, S.; Guo, L.; Wheeler, D. A.;
Zhang, J. Z.; Antoun, B. R.; Mao, S. S. *Energy Environ. Sci.* **2011**, 4, (10),
3889-3899.
42. Sayama, K.; Nomura, A.; Arai, T.; Sugita, T.; Abe, R.; Yanagida, M.; Oi, T.;
Iwasaki, Y.; Abe, Y.; Sugihara, H. *The Journal of Physical Chemistry B*
2006, 110, (23), 11352-11360.
43. Wang, G.; Ling, Y.; Lu, X.; Qian, F.; Tong, Y.; Zhang, J. Z.; Lordi, V.;
Rocha Leao, C.; Li, Y. *The Journal of Physical Chemistry C* **2013**, 117,
(21), 10957-10964.
44. Sivula, K. *The Journal of Physical Chemistry Letters* **2013**, 4, (10),
1624-1633.
45. Zhou, M.; Wu, H. B.; Bao, J.; Liang, L.; Lou, X. W.; Xie, Y. *Angew.*
Chem. Int. Ed. **2013**, 52, (33), 8579-8583.
46. Abdi, F. F.; Han, L.; Smets, A. H. M.; Zeman, M.; Dam, B.; van de Krol, R.
Nat Commun **2013**, 4, 2195.

47. Su, J.; Guo, L.; Bao, N.; Grimes, C. A. *Nano Lett* **2011**, 11, (5), 1928-1933.
48. Iwase, A.; Kudo, A. *J Mater Chem* **2010**, 20, (35), 7536-7542.
49. Zhong, D. K.; Choi, S.; Gamelin, D. R. *J Am Chem Soc* **2011**, 133, (45), 18370-18377.
50. Su, J.; Guo, L.; Yoriya, S.; Grimes, C. A. *Cryst Growth Des* **2009**, 10, (2), 856-861.
51. Ye, H.; Lee, J.; Jang, J. S.; Bard, A. J. *The Journal of Physical Chemistry C* **2010**, 114, (31), 13322-13328.
52. Liang, Y.; Tsubota, T.; Mooij, L. P. A.; van de Krol, R. *The Journal of Physical Chemistry C* **2011**, 115, (35), 17594-17598.
53. Abdi, F. F.; van de Krol, R. *The Journal of Physical Chemistry C* **2012**, 116, (17), 9398-9404.
54. Wang, G.; Ling, Y.; Wheeler, D. A.; George, K. E. N.; Horsley, K.; Heske, C.; Zhang, J. Z.; Li, Y. *Nano Lett* **2011**, 11, (8), 3503-3509.
55. Ling, Y.; Wang, G.; Reddy, J.; Wang, C.; Zhang, J. Z.; Li, Y. *Angew. Chem.* **2012**, 124, (17), 4150-4155.
56. Lin, Y.; Zhou, S.; Sheehan, S. W.; Wang, D. *J. Am. Chem. Soc.* **2011**, 133, 2398-2401.
57. Lin, Y.; Yuan, G.; Sheehan, S.; Zhou, S.; Wang, D. *Energy Environ. Sci.* **2011**, 4, (12), 4862-4869.
58. Li, L.; Yu, Y.; Meng, F.; Tan, Y.; Hamers, R. J.; Jin, S. *Nano Lett* **2012**, 12,

- (2), 724-731.
59. Bjorksten, U.; Moser, J.; Gratzel, M. *Chem Mater* **1994**, 6, (6), 858-863.
60. Warren, S. C.; Voatchovsky, K.; Dotan, H.; Leroy, C. M.; Cornuz, M.; Stellacci, F.; Habert, C.; Rothschild, A.; Gratzel, M. *Nat. Mater.* **2013**, 12, (9), 842-849.
61. Kennedy, J. H.; Anderman, M.; Shinar, R. *J Electrochem Soc* **1981**, 128, (11), 2371-2373.
62. Cherepy, N. J.; Liston, D. B.; Lovejoy, J. A.; Deng, H. M.; Zhang, J. Z. *J Phys Chem B* **1998**, 102, (5), 770-776.
63. Klahr, B.; Gimenez, S.; Fabregat-Santiago, F.; Hamann, T.; Bisquert, J. *J Am Chem Soc* **2012**, 134, (9), 4294-4302.
64. Goncalves, R. H.; Lima, B. H. R.; Leite, E. R. *J Am Chem Soc* **2011**, 133, (15), 6012-6019.
65. Wang, H. L.; Turner, J. A. *J Electrochem Soc* **2010**, 157, (11), F173-F178.
66. Vayssieres, L.; Guo, J. H.; Nordgren, J. *J Nanosci Nanotechno* **2001**, 1, (4), 385-388.
67. Vayssieres, L.; Sathe, C.; Butorin, S. M.; Shuh, D. K.; Nordgren, J.; Guo, J. *H. Adv Mater* **2005**, 17, (19), 2320-+.
68. Glasscock, J. A.; Barnes, P. R. F.; Plumb, I. C.; Savvides, N. *Journal of Physical Chemistry C* **2007**, 111, (44), 16477-16488.
69. Hahn, N. T.; Mullins, C. B. *Chem Mater* **2010**, 22, (23), 6474-6482.

70. Kumari, S.; Singh, A. P.; Sonal; Deva, D.; Shrivastav, R.; Dass, S.; Satsangi, V. R. *Int J Hydrogen Energ* **2010**, 35, (9), 3985-3990.
71. Sartoretti, C. J.; Alexander, B. D.; Solarska, R.; Rutkowska, W. A.; Augustynski, J.; Cerny, R. *J Phys Chem B* **2005**, 109, (28), 13685-13692.
72. Pu, A.; Deng, J.; Li, M.; Gao, J.; Zhang, H.; Hao, Y.; Zhong, J.; Sun, X. *Journal of Materials Chemistry A* **2014**, 2, (8), 2491-2497.
73. Liu, J.; Liang, C.; Zhang, H.; Tian, Z.; Zhang, S. *The Journal of Physical Chemistry C* **2012**, 116, (8), 4986-4992.
74. Franking, R.; Li, L.; Lukowski, M. A.; Meng, F.; Tan, Y.; Hamers, R. J.; Jin, S. *Energy Environ. Sci.* **2013**, 6, (2), 500-512.
75. Shen, S.; Kronawitter, C. X.; Wheeler, D. A.; Guo, P.; Lindley, S. A.; Jiang, J.; Zhang, J. Z.; Guo, L.; Mao, S. S. *Journal of Materials Chemistry A* **2013**, 1, (46), 14498-14506.
76. Cesar, I.; Sivula, K.; Kay, A.; Zboril, R.; Graetzel, M. *Journal of Physical Chemistry C* **2009**, 113, (2), 772-782.
77. Liang, Y. Q.; Enache, C. S.; van de Krol, R. *Int J Photoenergy* **2008**.
78. Satsangi, V. R.; Kumari, S.; Singh, A. P.; Shrivastav, R.; Dass, S. *Int J Hydrogen Energ* **2008**, 33, (1), 312-318.
79. Zhang, M.; Luo, W.; Li, Z.; Yu, T.; Zou, Z. *Appl. Phys. Lett* **2010**, 97, 042105.
80. Jang, J. S.; Lee, J.; Ye, H.; Fan, F. R. F.; Bard, A. J. *Journal of Physical*

- Chemistry C* **2009**, 113, (16), 6719-6724.
81. Gaudon, M.; Pailhe, N.; Majimel, J.; Wattiaux, A.; Abel, J.; Demourgues, A.
J Solid State Chem **2010**, 183, (9), 2101-2109.
82. Ingler, W. B.; Khan, S. U. M. *TSF* **2004**, 461, (2), 301-308.
83. Kleiman-Shwarsstein, A.; Hu, Y. S.; Forman, A. J.; Stucky, G. D.;
McFarland, E. W. *Journal of Physical Chemistry C* **2008**, 112, (40),
15900-15907.
84. Aroutiounian, V. M.; Arakelyan, V. M.; Shahnazaryan, G. E.;
Hovhannisyan, H. R.; Wang, H.; Turner, J. A. *SoEn* **2007**, 81, (11),
1369-1376.
85. Xi, L.; Chiam, S. Y.; Mak, W. F.; Tran, P. D.; Barber, J.; Loo, S. C. J.; Wong,
L. H. *Chemical Science* **2012**.
86. Jang, J. S.; Yoon, K. Y.; Xiao, X.; Fan, F.-R. F.; Bard, A. J. *Chem Mater*
2009, 21, (20), 4803-4810.
87. Ling, Y.; Wang, G.; Wheeler, D. A.; Zhang, J. Z.; Li, Y. *Nano Lett* **2011**, 11,
(5), 2119-2125.
88. Morrish, R.; Rahman, M.; MacElroy, J. M. D.; Wolden, C. A.
ChemSusChem **2011**, 4, (4), 474-479.
89. Uchiyama, H.; Yukizawa, M.; Kozuka, H. *The Journal of Physical
Chemistry C* **2011**, 115, (14), 7050-7055.

Chapter 2

Sn-doped Hematite Nanostructures for Photoelectrochemical Water

Splitting

Abstract

We report the synthesis and characterization of Sn-doped hematite nanowires and nanocorals as well as their implementation as photoanodes for photoelectrochemical water splitting. The hematite nanowires were prepared on a fluorine-doped tin oxide (FTO) substrate by a hydrothermal method, followed by high temperature sintering in air to incorporate Sn, diffused from the FTO substrate, as a dopant. Sn-doped hematite nanocorals were prepared by the same method, except tin(IV) chloride (SnCl_4) was added as the Sn precursor. X-ray photoelectron spectroscopy (XPS) analysis confirms Sn^{4+} substitution at Fe^{3+} sites in hematite, and Sn-dopant levels increase with sintering temperature. Sn-dopant serves as an electron donor and increases the carrier density of hematite nanostructures. The hematite nanowires sintered at 800 °C yielded a pronounced photocurrent density of 1.24 mA/cm^2 at 1.23 V vs. RHE, which is the highest value observed for one-dimensional hematite structures. In comparison to nanowires, Sn-doped hematite nanocorals exhibited smaller

feature sizes and increased surface areas. Significantly, they showed a remarkable photocurrent density of 1.86 mA/cm^2 at 1.23 V vs. RHE , which is approximately 1.5 times higher than the nanowires. Ultrafast spectroscopy studies revealed that there is significant electron-hole recombination within the first few picoseconds, while Sn-doping and surface morphology have no major effect on the ultrafast dynamics of the charge carriers on the picosecond time scales. The enhanced photoactivity in Sn-doped hematite nanostructures should be due to the improved electrical conductivity and increased surface area.

2.1 Introduction

Photoelectrochemical water splitting is a promising method of transforming solar energy into chemical energy stored in the form of hydrogen in an environmentally benign manner.^{1, 2} In the past decades, metal oxide semiconductors have been extensively studied as photoelectrodes for water splitting.^{1, 3-8} Among different metal oxide materials, hematite ($\alpha\text{-Fe}_2\text{O}_3$) has attracted a lot of attention^{4, 9-24} due to its favorable optical bandgap (2.2 eV), extraordinary chemical stability in oxidative environment, abundance, and low-cost. However, the photoelectrochemical activity of hematite is limited by several key factors such as relatively poor absorptivity,²⁵ very short excited-state lifetime ($\sim 10^{-12} \text{ s}$),²⁶ poor oxygen evolution reaction kinetics,²⁷ and a short hole diffusion length (2–4 nm).²⁰

To address these limitations and improve solar conversion efficiency, enormous efforts have been focused on the development of hematite nanostructures and the modification of their electronic structure via elemental doping.^{9, 11, 13, 15, 20, 28} Hematite nanostructures with an increased semiconductor/electrolyte interface and reduced diffusion length for minority carriers are expected to be more efficient in charge carrier collection.^{9, 11, 19, 20} It has recently been reported that a cauliflower-type hematite nanostructure was prepared by atmosphere pressure chemical vapor deposition (APCVD), which showed improved photocurrent.²¹ On the other hand, hematite structures have been doped with different elements such as Si,^{25, 29-31} Ti,^{15, 18, 29, 32} Al,^{32, 33} Mg,^{13, 16} Zn,^{31, 32} Mo,³⁴ Cr,³⁴ and Sn.^{13, 33} Dopants can play distinct roles in enhancing PEC activity of semiconductor materials. For example, dopants such as Ti⁴⁺ have been reported as an electron donor by substitutionally replacing Fe³⁺ and reducing Fe³⁺ to Fe²⁺.^{15, 32} It can improve the electrical conductivity of hematite via a polaron hopping mechanism.^{29, 35} Nevertheless, Si-doped hematite nanocrystalline films prepared by APCVD produced a benchmark photocurrent density of 2.7 mA/cm² at 1.23 V vs. RHE under a simulated solar light of 100 mW/cm², which was substantially higher than that of undoped hematite.^{25, 29-31} Si as a dopant was believed to lead to the formation of hematite dendrites with substantially increased surface area, which reduced the hole diffusion length and thereby the electron-hole recombination. Recently, Sivula *et al.* have reported a

mesoporous hematite structure with pronounced photocurrent density.²⁰ Significantly, they observed that Sn diffused from the FTO substrate into the mesoporous hematite film when the substrate was sintered at a high temperature (800 °C). The incorporation of Sn caused a two-fold enhancement in the optical absorption coefficient as a result of the structural distortion of the hematite lattice. The unintentional Sn doping was believed to play an important role in the enhanced photoactivity of hematite. Despite that, the effect of Sn doping in hematite nanostructures is still not well understood. In this work, we report for the first time the growth of intentionally Sn-doped hematite nanostructures on a conducting substrate. We independently confirmed the Sn diffusion from the FTO substrate reported in the Sivula *et al.* paper, and further investigated the effect of Sn doping on the morphology and electronic properties of hematite nanostructures using photoelectrochemical measurements and ultrafast laser spectroscopy.

2.2 Experimental Section

Synthesis of hematite nanostructures: Hematite nanowires were prepared on a fluorine-doped tin oxide (FTO, TEC 15, Pilkington glass) glass substrate by a modified procedure based on Vayssieres *et al.*'s work.³⁶ A teflon-lined stainless steel autoclave was filled with 20 ml aqueous solution containing 0.15 M of ferric chloride ($\text{FeCl}_3 \cdot 6\text{H}_2\text{O}$, Acros, 99+%) and 1 M sodium nitrate (NaNO_3 ,

Fisher 99.4%) at pH 1.5 (adjusted by HCl). A piece of FTO glass slide, washed with acetone, ethanol, and then deionized water, was put into the autoclave and heated at 95 °C for 4 hr. A uniform layer of iron oxyhydroxides (FeOOH) film (yellow color) was formed on the FTO substrate. The FeOOH-coated substrate was then washed with deionized water to remove any residual salt, and subsequently sintered in air at 550 °C for 2 hr. During the sintering process, the FeOOH nanowires were converted into hematite nanowires. For photoelectrochemical measurements, hematite nanowires were annealed at various temperatures in a range from 550 to 850 °C for additional 20 min. Heating ramp rate was 100 °C /min.

Sn-doped hematite nanocorals were prepared by the same procedure for undoped hematite nanowires, except 1 ml tin(IV) chloride (SnCl₄) ethanol solution (10 mg/ml) was added as the tin precursor into the solution mixture.

Structural characterization: The hematite nanostructured films on FTO substrate were characterized by PXRD with a Rigaku Americas Miniflex Plus powder diffractometer. Diffraction patterns were recorded from 20 to 80° 2θ with a step size of 0.04° at 1°/min.

Fabrication and PEC measurement of hematite nanostructured photoanodes: Hematite nanostructures were fashioned into photoanodes by

securing a copper wire onto a bare portion of FTO substrate by soldering. The substrate was then sealed on all edges with epoxy resin except for a working area of 0.12 cm^2 .

All PEC measurements were carried out in a three-electrode electrochemical cell utilizing a coiled Pt wire as a counter electrode and an Ag/AgCl electrode as a reference. The Electrolyte was an aqueous solution of NaOH with a pH of 13.6, deaerated by purging N_2 gas into electrolyte. All *J-V* measurements were recorded by an electrochemical workstation (Model CHI 660D, CH instruments, Inc., Austin, TX); and a solar simulator (Newport, Model 69907) coupled to a filter (AM 1.5G) using a 150 W Xenon lamp as the white light source. The light power density of 100 mW/cm^2 was measured with a power meter (Molelectron, PM5100). IPCE characteristics were measured with a monochromator (Oriel Cornerstone 130 1/8m). Electrochemical impedance data were measured at 10 kHz under the same condition as *J-V* dark scan.

Ultrafast Studies of Photoexcited Electron Dynamics: The ultrafast laser system is based on a Quantronix-designed femtosecond laser system, which consists of an Er-doped fiber oscillator, a regenerative/multi-pass amplifier, and a diode-pumped, Q-switched, second harmonic Nd:YLF pump laser (527 nm, 10 W capacity). Before injection into the amplifier, chirped pulse amplification was performed to temporally stretch, amplify, and recompress the initial short pulse,

resulting in a pulse near its original duration, yet with a vastly higher energy level. After amplification, the as-generated fundamental (795 nm) was beam-split to generate both a white light continuum (WLC) probe pulse as well as feeding a tunable optical parametric amplifier (OPA) that consists of two delay stages: a signal pre-amplification stage and a power amplification stage. The output of the OPA was passed through wavelength separators in order to achieve a tunable pump wavelength. The system operates at 750 Hz repetition rate. The final output was ~130 fs pulses, with a power output of ~100 nJ/pulse at the sample, centered at 540 nm excitation wavelength which was attenuated with neutral density filters. The pump beam was overlapped spatially and temporally with the WLC probe beam at the sample. The time delay between the pump and probe beams was controlled by a translation stage with 1 μm resolution. Each sample was tested for six cycles to achieve a lower-noise average response.

2.3 Results and Discussion

Hematite nanowires were synthesized on a FTO glass substrate using a modified hydrothermal method based on Vayssieres *et al.*'s work (Experimental Sections).³⁶ A uniform layer of iron oxyhydroxides (FeOOH) nanowire film (yellow color) was formed on a FTO substrate after heating the substrate in an aqueous solution containing 0.15 M FeCl_3 at 95 °C for 4 hours. These FeOOH-coated substrates were sequentially sintered in air at 550 °C for 2 hours

to obtain hematite nanowires. The film's color changed from yellow to red after sintering, suggesting successful conversion from FeOOH to α -Fe₂O₃. Scanning electron microscopy (SEM) image (Figure 2.1a) showed that the red film was covered by nanowires with a diameter of about 60 nm and an average wire length of 700 nm. Powder X-ray diffraction (XRD) data obtained from these nanowire films can be indexed to the characteristic peaks of hematite (JCPDS 33-0664) (Figure 2.1c), after subtracting the diffraction peaks originated from the FTO substrate. The absence of FeOOH diffraction peaks indicates the complete conversion of FeOOH to α -Fe₂O₃. Strong (110) diffraction implies these hematite nanowires are highly oriented in [110] direction on the substrate, which further suggested the growth axis of these nanowires should be along [110]. Importantly, it has been reported that hematite has a strong anisotropic conductivity; four orders of magnitude higher along the [110] direction than orthogonal to them.^{11, 35} It facilitates the collection of photoexcited electrons along the nanowire axis via hopping through Fe^{II}/Fe^{III} mixed valence structure.³⁵ To induce the diffusion of Sn from the FTO layer into the hematite, the nanowire films were further sintered at 600, 650, 700, 800 and 850 °C for an additional 20 min. The SEM image (Figure 2.1b) together with the XRD results (Figure 2.1c) revealed that neither the structure nor the crystal phase of the hematite nanowires changed after high-temperature sintering. The diameters of nanowires were slightly increased to ~80 nm after sintering at 800 °C, possibly due to

aggregation in the sintering process.

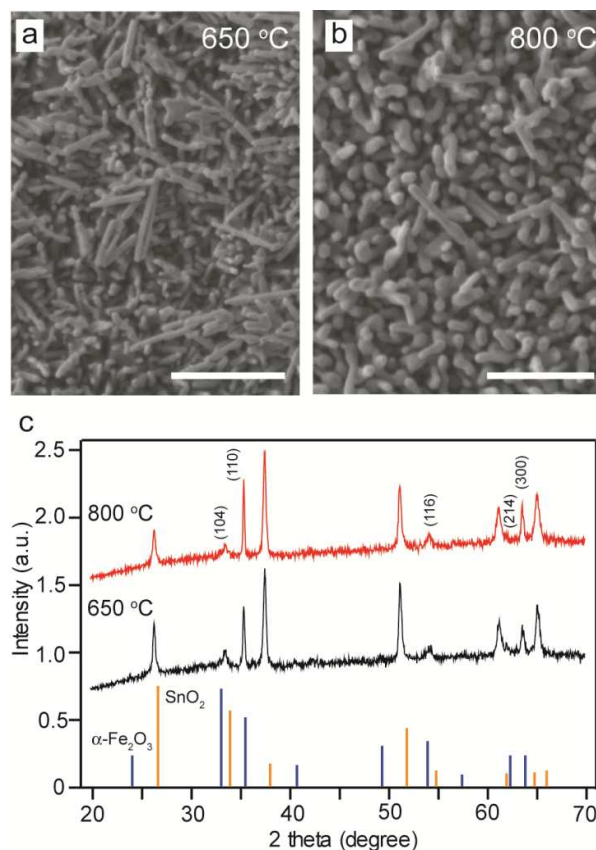


Figure 2.1 SEM images of hematite nanowires sintered at (a) 650 °C and (b) 800 °C. Scale bars are 1 μm. (c) XRD spectra collected for hematite nanowires sintered at 650 and 800 °C. The blue and orange lines highlighted the diffraction peaks of $\alpha\text{-Fe}_2\text{O}_3$ (JCPDS 33-0664) and SnO_2 (JCPDS 41-1445), respectively. The SnO_2 diffraction peaks originated from the FTO substrate.

To confirm the incorporation of Sn diffused from FTO substrate into hematite nanowires, X-ray photoelectron spectroscopy (XPS) analyses were performed on each sample. The Sn 3d XPS data are briefly summarized in Table 2.1. While Sn was not detected in FeOOH or as-prepared hematite nanowires, the results confirmed the presence of Sn doping in all hematite samples sintered

at temperatures at or above 650 °C (Figure 2.2a). The Sn/(Sn+Fe) atomic ratios (Sn%) of these unintentionally Sn-doped hematite nanowire samples increased with sintering temperature. Although the hematite nanowires annealed at 850 °C yielded the highest Sn% of 11.1%, the sintering at 850 °C caused severe distortion of the glass substrate and the FTO layer became insulating. High-resolution Sn 3d XPS spectra of each unintentionally Sn-doped hematite nanowire sample exhibited two peaks centered at 495.1 and 486.4 eV, corresponding to Sn 3d_{3/2} and Sn 3d_{5/2} peaks (Figure 2.2b). The binding energy of Sn 3d_{5/2} (486.4 eV) is between the typical values for SnO₂ (486.6 eV) and metallic Sn (484.6 eV),³⁷ and indicates that the Sn⁴⁺ dopants are substitutionally incorporated at the Fe³⁺ sites in the hematite lattice.

Table 2.1 Summary of Sn 3d XPS data for FeOOH, undoped and Sn-doped hematite samples

Sample	FeOOH	Undoped hematite nanowires						Sn-doped hematite nanocorals	
Temperature	-	550	600	650	700	800	850	650	800
Sn %	0	0	0	1.1	0.9	9.9	11.1	5.516	9.412

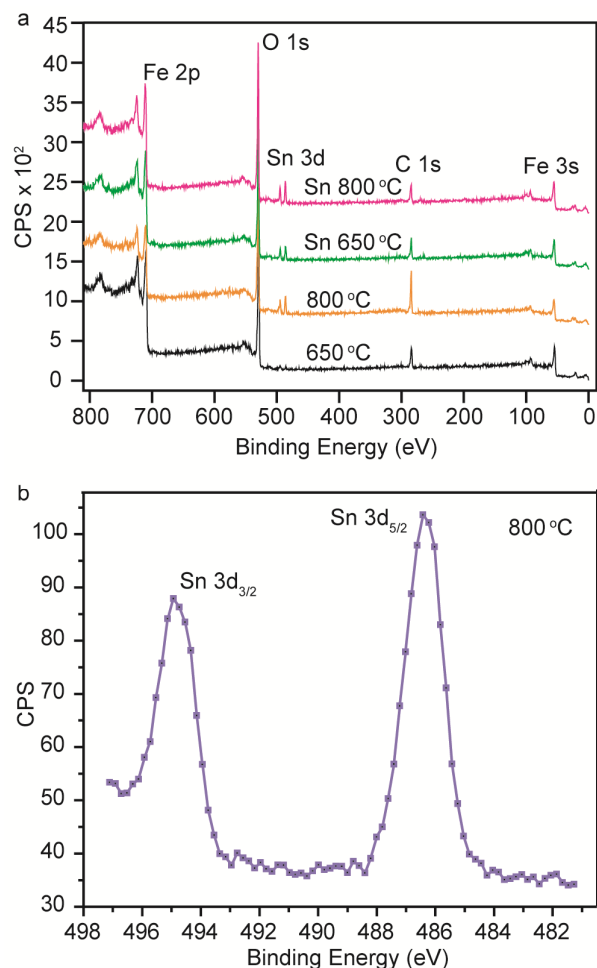


Figure 2.2 (a) XPS survey of hematite nanowires and nanocorals sintered at 650 and 800 °C. (b) High-resolution Sn 3d XPS spectra of hematite nanowires

Photoelectrochemical measurements were performed in a three-electrode electrochemical cell using hematite nanostructures on FTO as working electrode, a platinum coil as counter electrode and a reference of Ag/AgCl. The photocurrent density-applied potential (J - V) scans for hematite nanowire photoanodes, sintered at various temperatures, were measured in 1M NaOH electrolyte (pH 13.6) deaerated by purging nitrogen gas into electrolyte, in the

dark and with the AM 1.5G simulated solar light at 100 mW/cm² (Figure 3.3a). The measured potentials vs. Ag/AgCl were converted to the reversible hydrogen electrode (RHE) scale according to the Nernst equation,

$$E_{\text{RHE}} = E_{\text{Ag/AgCl}} + 0.059 \text{ pH} + E^{\circ}_{\text{Ag/AgCl}}$$

where E_{RHE} is the converted potential vs. RHE, $E^{\circ}_{\text{Ag/AgCl}} = 0.1976 \text{ V}$ at 25 °C, and $E_{\text{Ag/AgCl}}$ is the experimentally measured potential against Ag/AgCl reference. The as-prepared hematite nanowires (sintered at 550 °C) yielded a relatively low photocurrent density of 0.035 mA/cm² at 1.23 V vs. RHE. Significantly, the photocurrent densities of these hematite nanowires drastically increased with sintering temperature (Figure 2.3a). The onset temperature was 650 °C (Figure 2.3a, inset), which was consistent with the increase of Sn%. This result suggested a strong correlation between Sn% and photocurrent density of hematite. The sudden drop of photocurrent for the hematite nanowires sintered at 850 °C can be ascribed to the considerably increased resistivity of FTO substrate. In addition, the onset of dark scans were shifted to more positive potential, as the resistivity of FTO substrate increased with sintering temperature. The hematite nanowires sintered at 800 °C exhibited a pronounced photocurrent density of 1.24 mA/cm² at 1.23 V vs. RHE, and reached a maximum photocurrent density of 1.95 mA/cm² at 1.6 V vs. RHE. To our knowledge, this is the highest photocurrent density observed for hematite nanowires. All

hematite nanowires sintered at various temperatures showed similar turn-on voltage around 0.6-0.7 V vs. RHE. This voltage is relatively low compared to the typical values ranging from 0.8 to 1.0 V observed in other hematite structures without catalyst^{11, 15, 20}, thus, improving the photocurrent at lower bias voltage. Similar turn-on voltage was obtained in the previously reported hematite nanowires prepared by the same method using FeCl₃ precursor³⁸. The shift might be related to the growth method and possibly the morphology of hematite structure, although further studies are necessary to elucidate the reason.

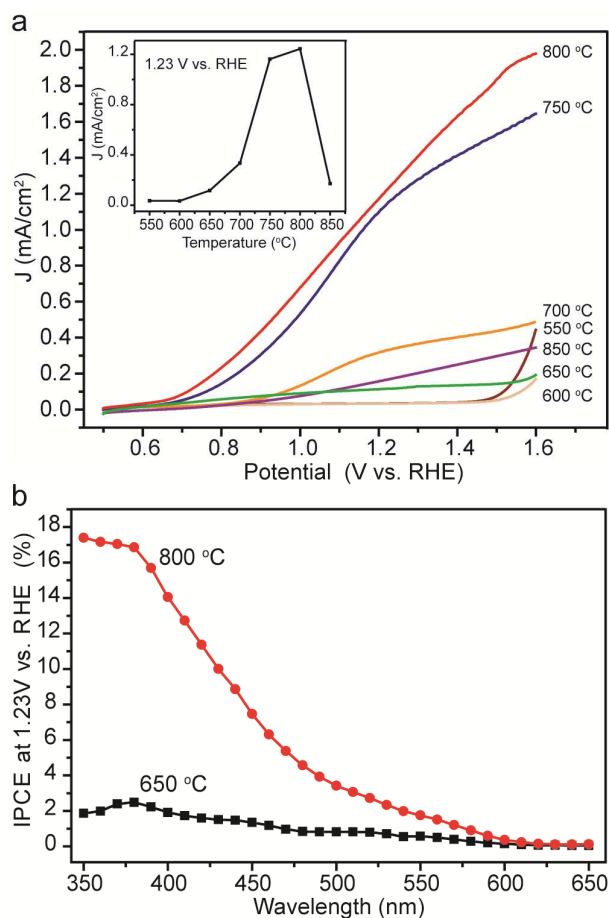


Figure 2.3 (a) J - V scans collected for hematite nanowire photoanodes sintered at different temperatures, with a scan rate of 10 mV/s. All samples were measured in 1M NaOH electrolyte (pH 13.6) with the AM 1.5G simulated solar light at 100 mW/cm². Inset: photocurrent densities at 1.23 V vs. RHE are plotted as a function of sintering temperature. (b) IPCE spectra of hematite nanowire samples sintered at 650 and 800 °C, collected at the incident wavelength range from 350 to 650 nm at a potential of 1.23 V vs. RHE.

Incident-photon-to-current-efficiencies (IPCE) for unintentionally Sn-doped hematite nanowires sintered at 650 and 800 °C were measured at 1.23 V vs. RHE as a function of incident light wavelength (Figure 2.3b). IPCE is expressed as $IPCE = (1240 \cdot I) / (\lambda \cdot J_{light})$, where I is the photocurrent density (mA/cm²), λ the incident light wavelength (nm), and J_{light} (mW/cm²) is the power density of monochromatic light at specific wavelength. The hematite nanowires sintered at 800 °C showed substantially enhanced IPCE values compared to the sample annealed at 650 °C at all measured wavelengths, which are consistent with their J - V characteristics. Their IPCE dropped to zero at wavelengths above 610 nm, which shows that the optical bandgap of these hematite nanowires is ca. 2 eV. The observed enhanced photocurrent density could be ascribed to the improved absorption coefficient of hematite as reported in the Sivula *et al.* work,²⁰ as well as the increased electrical conductivity as substitutional Sn-doping is expected to act as an electron donor.

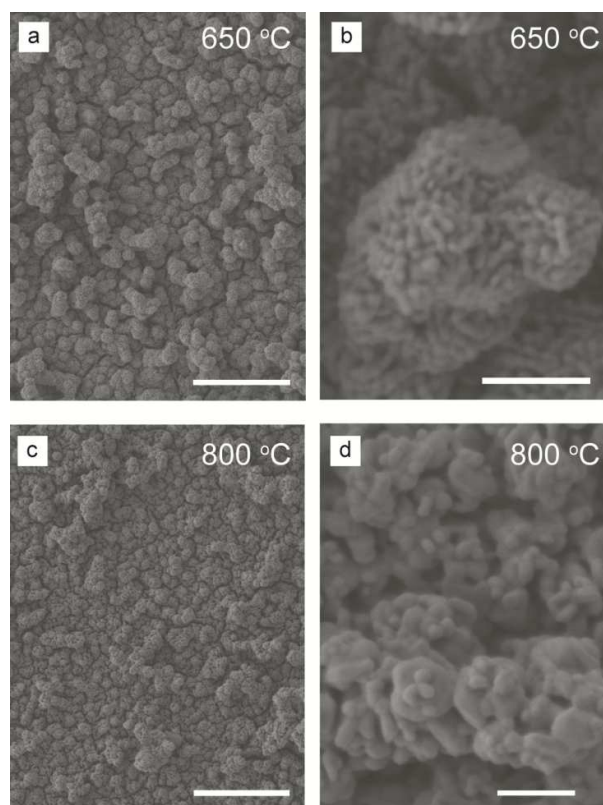


Figure 2.4 SEM images of hematite nanocorals sintered at (a, b) 650 °C and (c, d) 800 °C. Scale bars are 4 μm in (a, c) and 400 nm in (b, d).

Based on the above experiments, we confirmed the Sn diffusion from FTO substrate, as first reported in Sivula *et al.* paper, and substantially enhanced the photoactivity of hematite nanowires for water splitting. Despite that high-temperature sintering can introduce Sn from the FTO substrate into hematite, and the loss of Sn will considerably degrade the electrical conductivity of the FTO substrate and it is certainly not ideal to limit the hematite growth on the FTO substrate. Moreover, to understand the effect of Sn doping on the photoelectrochemical performance of hematite, a better control of Sn doping is

necessary. Here we report for the first time the synthesis of hematite nanostructures on a conducting substrate with controlled Sn doping. The Sn-doped hematite samples were prepared in conditions similar to that of the undoped samples (Experimental Sections), except hydrated tin(IV) chloride ($\text{SnCl}_4 \cdot x\text{H}_2\text{O}$) dissolved in ethanol solution (10 mg SnCl_4 in 1 ml ethanol) was used as the Sn precursor. A control sample prepared in the same amount of ethanol solution without SnCl_4 was made for comparison. SEM image (Figure 2.4a and b) revealed the formation of coral-like nanostructures constituted by small nanorods, with an average diameter of ~ 40 nm and a length of ~ 100 nm, in the Sn-doped sample. High-temperature sintering at 800°C caused a small increase in the size of rod-like structures in the nanocorals as a result of aggregation (Figure 2.4c and d). The control sample showed unique morphology that is different from both the undoped hematite nanowires and Sn-doped nanocorals (Figure 2.5a and b). It confirmed that the drastic morphological change from nanowire to nanocoral was due to the presence of ethanol solution and Sn-doping. XRD data confirmed the ethanol solution and Sn-doping did not change the hematite crystal structure, while the diffraction patterns changes due to the morphological change of material, as expected (Figure 2.5c).

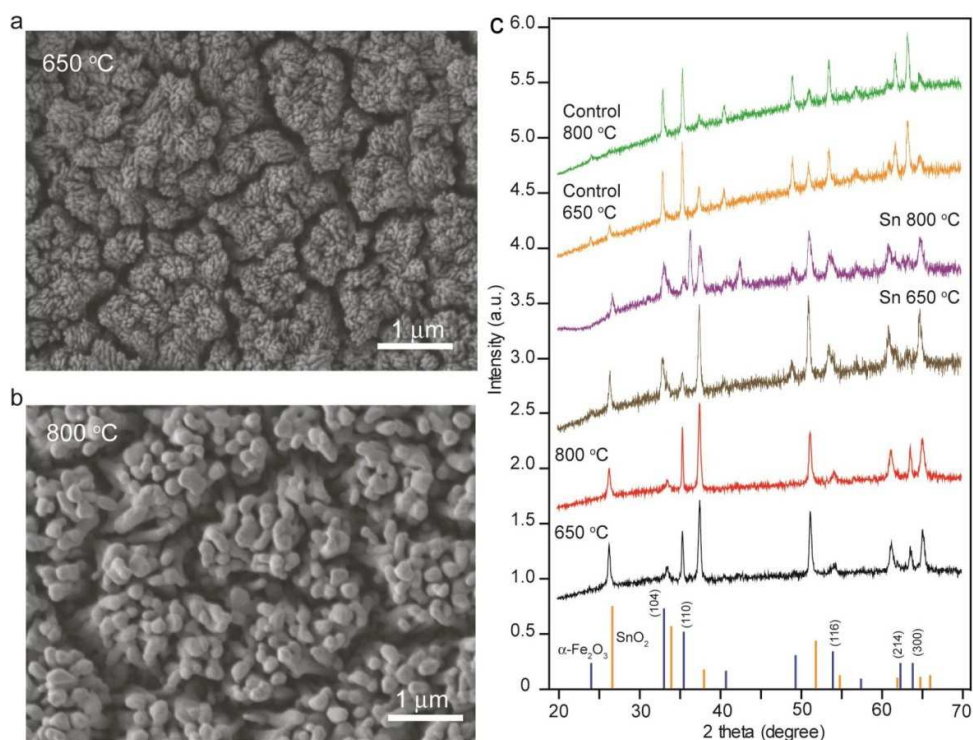


Figure 2.5 SEM images of hematite nanostructures prepared in the presence of ethanol solution (without SnCl_4). These samples were sintered at (a) 650 °C and (b) 800 °C. (c) XRD spectra collected for hematite nanowires, nanocorals and control samples sintered at 650 and 800 °C. The blue and orange lines highlighted the diffraction peaks of $\alpha\text{-Fe}_2\text{O}_3$ and SnO_2 , respectively. Their characteristic diffraction peaks were identified and can be indexed to $\alpha\text{-Fe}_2\text{O}_3$ structure (JCPDS 33-0664). The SnO_2 peaks are believed to be originating from the FTO substrate.

XPS data collected from Sn-doped samples offers direct evidence of Sn incorporation in hematite nanocorals. As shown in Table 1, the Sn% of hematite nanocoral sintered at 650 °C (5.5%) is five times higher compared to the relevant hematite nanowire sample, confirming the successful preparation of intentionally Sn-doped hematite. On the other hand, the Sn-doped hematite nanocoral film sintered at 800 °C has comparable Sn% (9.4%) with the undoped

sample (9.9%). In comparison to Sn-doped nanocoral sintered at 650 °C, the additional ~4 % Sn-doping is expected due to the Sn diffusion from FTO substrate. While the Sn precursor substantially increases Sn% in hematite at lower sintering temperature, the maximum level of Sn% seems to be intrinsically limited by the sintering temperature and hematite structure, even in the presence of excess Sn precursor.

The *J-V* curves for Sn-doped hematite nanocorals, sintered at 650 and 800 °C, were measured under the same conditions as undoped samples. In comparison to hematite nanowires, the Sn-doped hematite nanocorals sintered at 650 °C showed a remarkable 8-fold enhancement in photocurrent density, up to 0.94 mA/cm² at 1.23 V *vs.* RHE (Figure 2.6a). The enhanced photocurrent can be attributed to the increased Sn% as well as surface area in Sn-doped hematite nanocorals. This work demonstrated an important method to significantly enhance the photoelectrochemical performance of hematite under relatively low sintering temperatures. Significantly, the Sn-doped nanocoral sample sintered at 800 °C showed an even higher photocurrent density of 1.86 mA/cm² at 1.23 V *vs.* RHE, which is about 1.5 times higher than the unintentionally doped nanowire sample sintered at the same temperature. Hematite nanocorals showed a positive shift of photocurrent onset potential from 0.65 to 0.8 V *vs.* RHE, compared to nanowire samples. This positive shift indicates the water oxidation

kinetics is limited possibly due to the increased surface trapping states as a result of increased surface area. Similar shift of photocurrent onset potential has been observed for other hematite structures.^{9, 19} The shift can be addressed by coupling the hematite nanocorals with an efficient oxygen evolving catalyst, and we anticipate that hematite nanocorals can achieve even higher photocurrent density at the same potential.

While the nanocorals and nanowires sintered at 800 °C have comparable Sn%, the considerable difference of photocurrent density observed in these two samples indicates that Sn-doping is not the only reason for the increased photocurrent. In comparison to nanowires, nanocorals have smaller feature size and an increased surface area that facilitated the diffusion of photoexcited holes and thereby reduced the electron-hole recombination. This is consistent with the recent report on an encapsulated hematite porous photoanode that showed a significant increase in water oxidation photocurrent.⁹ IPCEs were collected at 1.23 V *vs.* RHE for Sn-doped hematite nanocorals sintered at 650 and 800 °C (Figure 2.6b). In comparison to the undoped nanowire samples sintered at the same temperatures, Sn-doped hematite nanocorals showed uniformly higher IPCE values in the whole visible region. The results are consistent with the differences of photocurrent densities observed in the undoped and Sn-doped samples. At comparable photocurrents, the IPCE values at visible region (*e.g.*

500 nm) obtained from these hematite films are relatively low compared to the previously reported IPCE collected at the same bias.^{21,24} This could be due to the differences of the lamp power output at various wavelengths in each labs.

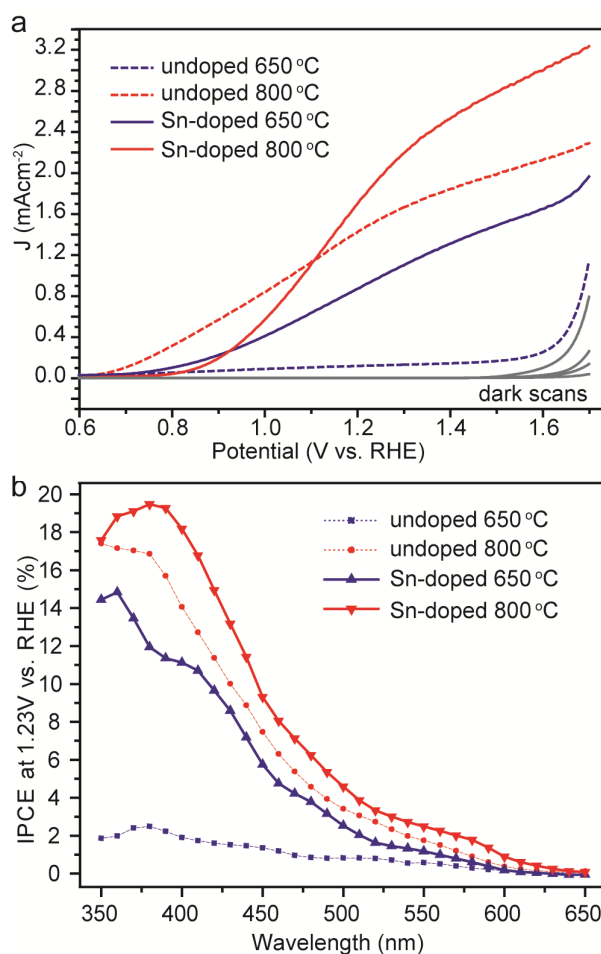


Figure 2.6 (a) Comparison of J - V scans collected for hematite nanocorals (solid lines) and nanowires (dashed lines) sintered at 650 and 800 °C, with a scan rate of 10 mV/s, in 1M NaOH electrolyte (pH 13.6) with the AM 1.5G simulated solar light at 100 mW/cm². (b) Comparison of IPCEs for hematite nanocorals (solid lines) and nanowires (dashed lines) sintered at 650 and 800 °C, collected at the incident wavelength range from 350 to 650 nm at a potential of 1.23 V vs. RHE.

PEC measurements were performed to study the photoelectrochemical properties of the photoanodes fabricated from double-sided, CdS and CdSe co-sensitized ZnO NW arrays. All PEC measurements were carried out in a three-electrode electrochemical cell in a stirred solution bubbled with nitrogen, with a coiled Pt wire as a counter electrode and an Ag/AgCl electrode as a reference. A mixture of 0.25 M Na₂S and 0.35 M Na₂SO₃ aqueous solution was used as electrolyte and sacrificial reagent to maintain the stability of CdS and CdSe. The electrolyte had a pH of ~9.5 and the solution potential was about -0.56 V. I-V measurements were made on a Solartron 1280B potentiostat coupled to an infrared water-filter (Oriel no. 6127) using a 1000 W Xenon Arc Lamp as the white light source. The CdS QD sensitized ZnO NWs were faced towards the incident light in all PEC measurements. In order to allow light penetrates through the first layer, we intentionally reduced the loading of CdS QDs. The CdSe QD was in maximum loading for complete light absorption. For comparison, double-sided ZnO NWs (denoted as ZnO-ZnO), CdS QD sensitized ZnO NWs (denoted as CdS-ZnO-ZnO-CdS) and CdSe QD sensitized ZnO NWs (denoted as CdSe-ZnO-ZnO-CdSe) were prepared in similar growth and sensitization conditions, and used as control samples for measurements. Figure 3.6 shows a set of linear sweep voltammograms recorded from these NW photoanodes in dark and at illumination of 100 mW/cm² (AM 1.5). All samples showed small dark current density, in the order of 10⁻¹ to 10⁻³ mA/cm²

from -0.7 V to 0.4 V vs. Ag/AgCl. Only the dark scans of ZnO-ZnO and CdS-ZnO-ZnO-CdSe samples are plotted in Figure 2.6 for clarity. While all NW photoanode showed pronounced photoresponse under light illumination, QD sensitized NW samples exhibited substantially enhanced photocurrent compared to pristine ZnO NWs. This can be attributed to the improved visible light absorption by the QDs, as shown in UV-vis absorption studies (Figure 2.7). The results confirmed efficient interfacial charge transfer between CdS, CdSe QDs and ZnO NW. Significantly, the co-sensitized CdS-ZnO-ZnO-CdSe NW showed a maximum photocurrent density of $\sim 12 \text{ mA/cm}^2$ at 0.4 V, which is about two times larger than that of single sensitized samples (CdS-ZnO-ZnO-CdS and CdSe-ZnO-ZnO-CdSe). The data indicate that the incident light transmitted through the CdS-ZnO layer to the CdSe-ZnO layer at the back of the substrate and the light was absorbed by both layers. More importantly, there was a synergistic effect in the co-sensitized sample that led to the photocurrent enhancement.

To understand the role of Sn-doping on the electronic properties of hematite in electrolyte solution, we performed electrochemical impedance measurements in the dark to determine the capacitance of hematite nanostructures (Analytical Methods, Supporting Information). The carrier density and flatband potential at hematite/electrolyte interface can be estimated

by the Mott-Schottky equation¹⁵

$$1/C^2 = (2/e_0\epsilon\epsilon_0N_d)[(V-V_{FB})-kT/e_0]$$

where C is the specific capacitance (F/cm^2), e_0 is the electron charge, ϵ the dielectric constant of hematite, ϵ_0 the permittivity of vacuum, N_d the carrier density, V the electrode applied potential, V_{FB} the flatband potential, and kT/e_0 is a temperature-dependent correction term. Representative Mott-Schottky plots, collected from hematite nanowires and nanocorals at a frequency of 10 kHz are presented in Figure 3.7. In contrast to planar samples, they exhibit a nonlinear behavior due to the cylindrical geometry of the nanowires. By extrapolating the X-intercepts of the linear region in Mott-Schottky plots ($1/C^2$ vs. V), V_{FB} of hematite nanowires sintered at 650 and 800 °C were found to be ~0.47 and 0.49 V vs. RHE (Figure 2.7). The V_{FB} potentials are consistent with the values reported for other hematites.²¹ The V_{FB} of nanocorals was not able to be measured due to the strong nonlinearity of Mott-Schottky plots (Figure 2.7, inset).

According to the Mott-Schottky equation, the slope of the plots has an inverse relationship with the carrier density of semiconductor film.

$$N_d = (2/e_0\epsilon\epsilon_0)[d(1/C^2)/dV]^{-1}$$

The positive slopes indicated that hematite nanowires and nanocorals are n -type semiconductors. The slopes determined from the analysis of Mott-Schottky plot were used to estimate the donor densities. With a ϵ value of 80 for hematite,²⁵

the electron densities of hematite nanowires sintered at 650 and 800 °C were calculated to be 1.89×10^{19} and 5.38×10^{19} cm^{-3} . The carrier densities are comparable to the reported values for Si-doped hematite structures.²⁵ Significantly, both nanowire and nanocoral samples sintered at 800 °C showed substantially increased donor density compared to the samples sintered at 650 °C. These data provided direct evidence to support that the Sn-doping served as an electron donor, and the donor density increased with Sn% in hematite.

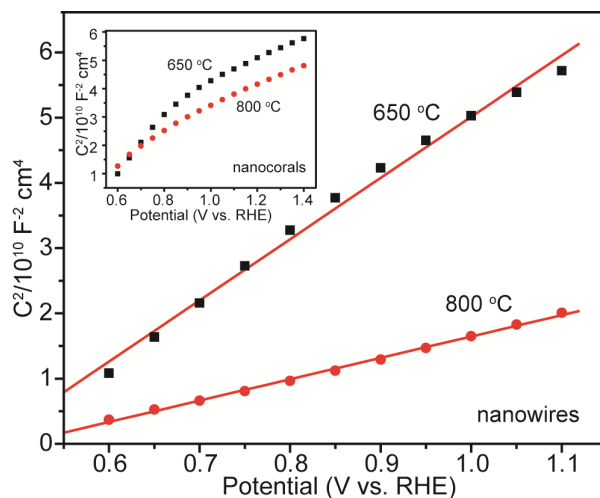


Figure 2.7 Mott-Schottky plots of hematite nanowires collected with a scan rate of 10 mV/s, in 1M NaOH electrolyte (pH 13.6), in the dark at a frequency of 10 kHz. Inset: Mott-Schottky plots of hematite nanocorals collected at the same conditions.

Ultrafast spectroscopy studies³⁹ were carried out to probe the fundamental charge carrier dynamics following photoexcitation and to understand the possible effect of Sn-doping and surface morphology on the

photoexcited electron dynamics in hematite. The ultrafast transient absorption profiles of hematite nanowires sintered at 650 and 800 °C are shown on three different time scales in Figure 3.8a-c. A pulse-width limited rise of the signal is followed by a decay that can only be fit to a multiple exponential. Two sets of very good curve fits were obtained using a triple exponential. The time constants for the 650 and 800 °C hematite nanowires are 0.362, 2.451 and 73.37 ps and 0.351, 2.304 and 67.4 ps, respectively. These time constants were convolved with a Gaussian (fwhm 130 fs) representing the cross-correlation of the pump and probe pulses. Several important features were disclosed by comparing the transient absorption decay profiles of the hematite samples. First, the overall charge carrier decays for hematite nanowires are very fast, without measurable transient absorption beyond 200 ps. The very fast decay is likely due to a high density of bandgap electronic states caused by internal defects and/or surface defects. This is consistent with the decay profiles reported previously for hematite nanoparticles.^{26,40} Second, hematite nanowires sintered at 650 °C showed relatively slower decay than those sintered at 800 °C (Figure 2.8a-c). The two hematite nanowire samples have similar structural morphology but different Sn%. Their similar dynamics features suggest Sn-doping has insignificant effect on the photoexcited electron dynamics, at least on the picosecond time scale. Finally, it is known that material morphology and surface area can affect the electron dynamics in semiconductor.⁴¹ In this regard, the

decay profiles of two hematite samples prepared in solution with and without ethanol were investigated and compared. These two samples were sintered at 650 °C have similar Sn%, but different morphology and surface area. As shown in Figure 6d, their decay profiles are essentially the same in both the 0-10 ps and 0-200 ps windows, indicating the effect of morphological change on the electron dynamics in hematite is negligible on the picosecond time scale. These dynamics data confirm that the increase of Sn% and/or surface area in the hematite nanostructures cannot reduce the rapid loss of photoexcited electron through different decay processes at very fast time scale. Therefore, the enhanced photoactivity observed in Sn-doped hematite nanowires and nanocorals is more likely due to the improved donor density and electrical conductivity. At the same Sn%, nanocorals with smaller feature size and higher surface area showed higher photocurrent density than the nanowires, possibly due to reduced diffusion length for holes. It remains a challenging problem to improve intrinsic electronic structure or reduce density of trap states of hematite materials, so that a longer photoexcited charge carrier lifetime and thereby more efficient charge separation can be achieved.

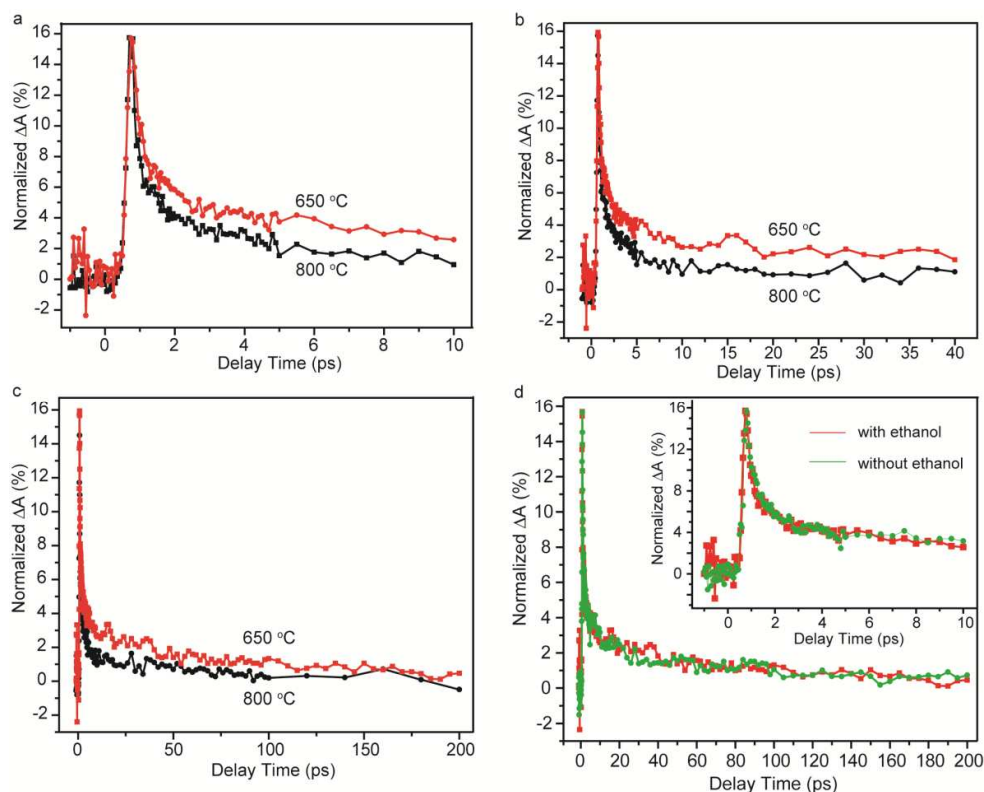


Figure 2.8 Ultrafast transient absorption decay profiles of hematite nanowires. (a) the 0-10 ps, (b) the 0-40 ps, and (c) the 0-200 ps windows are fit simultaneously using a nonlinear least-squares fitting algorithm to a triple-exponential decay convolved with a Gaussian representing the cross-correlation of the 540 nm pump (100 nJ/(pulse-cm²), attenuated with neutral density filters) and 620 nm probe pulses. The transient absorption has a pulse width limited rise time and is best fit to a triple exponential with 0.362, 2.451 and 73.37 ps and 0.351, 2.304 and 67.4 ps time constants for 650 and 800 °C samples respectively. (d) Normalized ultrafast transient absorption decay profiles (0-200 ps) of hematite nanowires sintered at 650 °C, prepared in the solution with (red line) and without (green line) ethanol. Inset: the same decay profiles in 0-10 ps window.

2.4 Conclusion

In summary, we have synthesized Sn-doped hematite nanowires and nanocorals on FTO substrate using hydrothermal method, followed by high-temperature sintering in air. In comparison to undoped hematite

nanostructures, these Sn-doped hematite nanostructures showed remarkable photocurrent densities as a result of improved carrier density and structural morphology due to Sn-doping. Further improvement of photoelectrochemical performance of these hematite nanostructures could potentially be achieved by optimizing the Sn dopant level at lower sintering temperatures and coupling them with efficient oxygen evolving catalysts. Moreover, ultrafast spectroscopy studies revealed that there is significant electron-hole recombination within the first few picoseconds, likely caused by a high density of bandgap states due to surface or internal defects, and there is a small amplitude, longer-lived component that is likely responsible for the photocurrent observed in photoelectrochemical measurement. Sn-doping and surface morphology have an insignificant effect on early time dynamics of the photoexcited charge carriers but important influence on the photoelectrochemical results, indicating that their effects are important mainly on the longer time scale. The future research efforts should focus on improving the intrinsic electronic structure of hematite nanomaterials, in order to achieve longer photoexcited charge carrier lifetime.

References

1. Grätzel, M. *Nature* **2001**, 414, (6861), 338-344.
2. Li, Y.; Zhang, J. Z. *Laser Photonics Rev.* **2010**, 4, (4), 517-528.
3. Liu, R.; Lin, Y.; Chou, L. Y.; Sheehan, S. W.; He, W.; Zhang, F.; Hou, H. J.

- M.; Wang D. *Angew. Chem. Int. Ed.*, **2011**, *50*, 499-502.
4. Sivula, K.; Le Formal, F.; Grätzel, M. *Chem. Mater.* **2009**, *21*, (13), 2862-2867.
 5. Lin, Y.; Zhou, S.; Liu, X. H.; Sheehan, S. W.; Wang, D. *J. Am. Chem. Soc.*, **2009**, *131*, 2772-2773.
 6. Wang, G. M.; Yang, X. Y.; Qian, F.; Zhang, J. Z.; Li, Y. *Nano Lett.* **2010**, *10*, (3), 1088-1092.
 7. Hensel, J.; Wang, G.; Li, Y.; Zhang, J. Z. *Nano Lett.* **2010**, *10*, 478-483.
 8. Yang, X. Y.; Wolcott, A.; Wang, G. M.; Sobo, A.; Fitzmorris, R. C.; Qian, F.; Zhang, J. Z.; Li, Y. *Nano Lett.* **2009**, *9*, (6), 2331-2336.
 9. Brilllet, J.; Grätzel, M.; Sivula, K. *Nano Lett.* **2010**, *10*, (10), 4155-4160.
 10. Cesar, I.; Kay, A.; Martinez, J. A. G.; Gratzel, M. *J. Am. Chem. Soc.* **2006**, *128*, (14), 4582-4583.
 11. Kay, A.; Cesar, I.; Grätzel, M. *J. Am. Chem. Soc.* **2006**, *128*, (49), 15714-15721.
 12. Frites, M.; Shaban, Y. A.; Khan, S. U. M. *Int. J. Hydrogen Energy* **2010**, *35*, (10), 4944-4948.
 13. Gaudon, M.; Pailhe, N.; Majimel, J.; Wattiaux, A.; Abel, J.; Demourgues, A. *J. Solid State Chem.* **2010**, *183*, (9), 2101-2109.
 14. Grätzel, M.; Kiwi, J.; Morrison, C. L.; Davidson, R. S.; Tseung, A. C. C. *J. Chem. Soc., Faraday Trans. I* **1985**, *81*, 1883-1890.

15. Hahn, N. T.; Mullins, C. B. *Chem. Mater.* **2010**, 22, (23), 6474-6482.
16. Ingler, W. B.; Khan, S. U. M. *Thin Solid Films* **2004**, 461, (2), 301-308.
17. Ingler, W. B.; Khan, S. U. M. *Electrochem. Solid-State Lett.* **2006**, 9, (4), G144-G146.
18. Kumari, S.; Singh, A. P.; Sonal; Deva, D.; Shrivastav, R.; Dass, S.; Satsangi, V. R. *Int. J. Hydrogen Energy* **2010**, 35, (9), 3985-3990.
19. Le Formal, F.; Grätzel, M.; Sivula, K. *Adv. Funct. Mater.* **2010**, 20, (7), 1099-1107.
20. Sivula, K.; Zboril, R.; Le Formal, F.; Robert, R.; Weidenkaff, A.; Tucek, J.; Frydrych, J.; Grätzel, M. *J. Am. Chem. Soc.* **2010**, 132, (21), 7436-7444.
21. Tilley, S. D.; Cornuz, M.; Sivula, K.; Grätzel, M. *Angew. Chem. Int. Ed.* **2010**, 49, (36), 6405-6408.
22. Wang, H. L.; Turner, J. A. *J. Electrochem. Soc.* **2010**, 157, (11), F173-F178.
23. Zhong, D. K.; Sun, J. W.; Inumaru, H.; Gamelin, D. R. *J. Am. Chem. Soc.* **2009**, 131, (17), 6086-6087.
24. Lin, Y.; S., Z.; Sheehan, S. W.; Wang, D. *J. Am. Chem. Soc.* **2011**, 133, 2398-2401.
25. Cesar, I.; Sivula, K.; Kay, A.; Zboril, R.; Grätzel, M. *J. Phys. Chem. C* **2009**, 113, (2), 772-782.
26. Cherepy, N. J.; Liston, D. B.; Lovejoy, J. A.; Deng, H. M.; Zhang, J. Z. *J. Phys. Chem. B* **1998**, 102, (5), 770-776.

27. Dareedwards, M. P.; Goodenough, J. B.; Hamnett, A.; Trevellick, P. R. *Chem. Soc., Faraday Trans. I* **1983**, 79, 2027-2041.
28. Hu, Y. S.; Kleiman-Shwarscstein, A.; Forman, A. J.; Hazen, D.; Park, J. N.; McFarland, E. W. *Chem. Mater.* **2008**, 20, (12), 3803-3805.
29. Glasscock, J. A.; Barnes, P. R. F.; Plumb, I. C.; Savvides, N. *J. Phys. Chem. C* **2007**, 111, (44), 16477-16488.
30. Liang, Y. Q.; Enache, C. S.; van de Krol, R. *Int. J. Photoenergy* **2008**, 739864.
31. Satsangi, V. R.; Kumari, S.; Singh, A. P.; Shrivastav, R.; Dass, S. *Int. J. Hydrogen Energy* **2008**, 33, (1), 312-318.
32. Sartoretti, C. J.; Alexander, B. D.; Solarska, R.; Rutkowska, W. A.; Augustynski, J.; Cerny, R. *J. Phys. Chem. B* **2005**, 109, (28), 13685-13692.
33. Jang, J. S.; Lee, J.; Ye, H.; Fan, F. R. F.; Bard, A. J. *J. Phys. Chem. C* **2009**, 113, (16), 6719-6724.
34. Kleiman-Shwarscstein, A.; Hu, Y. S.; Forman, A. J.; Stucky, G. D.; McFarland, E. W. *J. Phys. Chem. C* **2008**, 112, (40), 15900-15907.
35. Iordanova, N.; Dupuis, M.; Rosso, K. M. *J. Chem. Phys.* **2005**, 122, 144305.
36. Vayssieres, L.; Beermann, N.; Lindquist, S. E.; Hagfeldt, A. *Chem. Mater.* **2001**, 13, (2), 233-235.
37. Cao, Y.; He, T.; Zhao, L.; Wang, E.; Yang, W.; Cao, Y. *J. Phys. Chem. C* **2009**, 113, 18121-18123.

38. Lindgren, T.; Wang, H.; Beermann, N.; Vayssieres, L.; Hagfeldt, A.; Lindquist, S. *Sol. Energy Mater. Sol. Cells* **2002**, 71, 231–243.
39. Newhouse, R.; Wang, H.; Hensel, J.; Wheeler, D.; Zou, S.; Zhang, J. Z. *J. Phys. Chem. Lett.* **2011**, 2, 228-235.
40. Joly, A. G.; Williams, J. R.; Chambers, S. A.; Xiong, G.; Hess, W. P.; Laman, D. M. *J. Appl. Phys.* **2006**, 99, 053521.
41. Zhang, J. Z. *J. Phys. Chem. B* **2000**, 104, 7239-7253.

Chapter 3

The Influence of Oxygen Content on Thermal Activation of Hematite

Nanowires

Abstract

We report the studies of the influence of oxygen content on thermal activation of hematite nanowire-arrayed photoanodes for photoelectrochemical water oxidation. Highly photoactive hematite nanowires were prepared by thermal decomposition of akaganeite (β -FeOOH) nanowires at 550 °C in oxygen deficient ($N_2 + \text{air}$) atmosphere. In comparison to the hematite sample prepared in air, they yielded a substantially enhanced photocurrent density of 3.37 mA/cm² at 1.50 V vs. RHE, in 1 M NaOH electrolyte under front side illumination of simulated solar light (100 mW/cm² AM 1.5G), which is the best value reported for undoped hematite without oxygen evolving catalyst. The enhanced photoactivity is attributed to the improved donor density (one order of magnitude) of hematite nanowires as a result of formation of oxygen vacancies (Fe^{2+}). X-ray photoelectron spectroscopy analysis confirms the existence of Fe^{2+} in the hematite prepared in oxygen deficient environment. Mechanistic studies confirm that oxygen vacancies are formed via the dehydroxylation of

chloride-containing akaganeite in oxygen deficient atmosphere during thermal activation.

3.1 Introduction

Hematite (α -Fe₂O₃) is a promising photoelectrode material for solar-driven water splitting because its non-toxicity, abundance, chemical stability, low-cost, and favorable bandgap.¹⁻⁵ In comparison to the most studied metal oxide materials for photoelectrochemical (PEC) water splitting, including TiO₂,⁶⁻¹⁰ ZnO,¹¹ and WO₃,¹²⁻¹⁵ hematite has a favorable bandgap of ~2.1 eV, which accounts for a maximum theoretical solar-to-hydrogen (STH) efficiency of 15%.⁴ However, the reported STH efficiencies of hematite photoelectrodes are substantially lower than the theoretical value, due to several limiting factors such as poor conductivity, short excited-state lifetime (<10 ps),¹⁶ poor oxygen evolution reaction kinetics,¹⁷ low absorption coefficient,¹⁸ short diffusion length for holes (2-4 nm),¹⁹ and lower flat band potential in energy for water splitting.⁴ Enormous efforts have been made to overcome those limitations of hematite, including the incorporation of oxygen evolving catalysts to reduce kinetic barrier on hematite surface for water oxidation,²¹⁻²³ development of nanostructures to increase effective surface area and reduce diffusion length for carriers,^{4, 5, 24} as well as development of element-doped hematite for improving electrical conductivity and/or light absorption.²

Recently, we demonstrated that TiO₂ nanowires thermally treated in hydrogen showed increased donor density and PEC performance due to the increased donor density as a result of formation of oxygen vacancies.⁶ We anticipated that creating oxygen vacancy (V_o) and thereby Fe²⁺ sites in hematite could significantly increase its conductivity via a polaron hopping mechanism.^{25,}²⁶ Although V_o can be created by sintering hematite in a reductive atmosphere such as hydrogen, it may introduce H as a dopant into the structure. Additionally, hematite can be easily reduced in hydrogen to magnetite (Fe₃O₄), which is photo-inactive.²⁷ In this work, we report an alternative approach to prepare highly conductive and photoactive hematite through thermal decomposition of β-FeOOH in an oxygen-deficient atmosphere (N₂ + air). The as-grown hematite sample showed substantially enhanced photoactivity compared to the pristine hematite prepared in air. The oxygen content during thermal activation affects significantly the formation of V_o and thereby the photoactivity of hematite nanowires for water oxidation. This is the first demonstration of highly photoactive hematite nanowire arrays at relatively low activation temperature without element dopant.

3.2 Experimental section:

Preparation of Hematite nanowire arrays:

Hematite nanowire arrays were fabricated on a fluorine-doped tin oxide

(FTO, TEC 8, Hartford Glass Company Inc.) coated glass substrate based on a previously method with slight modification.²⁸ A Teflon-lined stainless steel autoclave of 30 mL capacity was filled with 20 mL aqueous solution containing 0.15 M of ferric chloride ($\text{FeCl}_3 \cdot 6\text{H}_2\text{O}$, Acros, 99+%) and 1 M sodium nitrate (NaNO_3 , Fisher 99.4%) at pH 1.5 (adjusted by HCl). A piece of FTO glass slide, washed with acetone, ethanol, and then deionized water, was put into the autoclave and heated at 95 °C for 4 hr in an oven and naturally cool down to ambient temperature. A uniform yellow layer of akaganeite ($\beta\text{-FeOOH}$) nanowire film was obtained on the FTO substrate. The akaganeite-coated substrate was then washed with deionized water and blown dry quickly with air, and subsequently sintered in air at 550 °C for 2 hr in a horizontal quartz-tube furnace. During the sintering process, the akaganeite nanowires were converted into red hematite nanowires. For those samples annealed in N_2 atmosphere, the tube furnace was first vacuumed to a pressure of 15 Torr, and then filled with ultrahigh purity N_2 (99.998%, Praxair). The sintering was carried out at 550 °C for 2 hr at 740 Torr pressure with a N_2 flow rate of 50 sccm.

Material Characterization:

The hematite nanowire films on FTO substrate were characterized by X-ray diffraction (XRD) with a Rigaku Americas Miniflex Plus powder diffractometer. Diffraction patterns were recorded from 10 to 80° 2 theta with a step size of 0.02° at 2° per minute. Scanning electron microscopy (SEM) images were collected

with a field-emission SEM (Hitachi S-4800 II). Raman spectra were collected with a Nicolet Almega XR Dispersive Raman Spectrometer (laser wavelength 780 nm). X-ray photoelectron spectroscopy (XPS) was collected by a RBD upgraded PHI-5000C ESCA system (Perkin-Elmer) using Mg-monochromatic X-ray at a power of 25 W with an X-ray-beam diameter of 10 mm, and a pass energy of 29.35 eV. The pressure of analyzer chamber was maintained below 5×10^{-8} Pa during the measurement. The binding energy was calibrated using the C 1s photoelectron peak at 284.6 eV as the reference.

Photoelectrochemical Measurements:

PEC measurements of the hematite samples as photoanodes were carried out in a three-electrode electrochemical cell using a coiled Pt wire as a counter electrode and an Ag/AgCl electrode as a reference electrode. An aqueous solution of 1 M NaOH with a pH 13.6 was used as the electrolyte, deaerated by purging N_2 gas into electrolyte. The substrate was sealed on all edges with epoxy resin except for an average working area of 0.15 cm^2 . All linear sweep voltammograms were measured by a CHI 660D electrochemical workstation (CH instruments, Inc., Austin, TX), with front side illumination using a solar simulator (Newport 69920, 1000 W xenon lamp) coupled with an infrared water filter (Oriel 6127) and an AM 1.5 global filter (Newport 81094). The power density of 100 mW/cm^2 was measured with a power meter (Molelectron, PM5100). Incident-photo-to-current-efficiencies (IPCE) were measured with the

same xenon lamp coupled with a monochromator (Oriel Cornerstone 130 1/8m).

3.3 Results and Discussion

Akaganeite nanowires were prepared through hydrolysis of FeCl_3 (0.15 M) in a high ionic strength (1 M NaNO_3), and low pH value (pH 1.5, adjusted by HCl) environment at 95 °C for 4 hr.²⁸ The as-prepared yellow film on FTO substrate was covered with nanowire arrays with average diameter and length of 70 nm and 700 nm, respectively (Figure 3.1a). X-ray diffraction (XRD) analysis (Figure 3.2) confirms the nanowires are $\beta\text{-FeOOH}$ (akaganeite, JCPDS 75-1594). The akaganeite-coated substrate was then washed by deionized water and sintered in an oxygen-deficient atmosphere (N_2 + air) at 550 °C for 2 hr to convert akaganeite into hematite with V_o (denoted as N-hematite). The oxygen-deficient atmosphere was achieved by vacuum the system down to a pressure of 15 Torr, and refilled with ultrahigh purity N_2 (99.998%, Praxair). The initial oxygen content is estimated to be 0.43 % ($\text{O}_2/(\text{O}_2+\text{N}_2)$, volume %). Hematite nanowires samples (denoted as A-hematite) were prepared by sintering the akaganeite film in air at 550 °C for 2 hr, as control. Thermal activation did not change the nanowire morphology (Figure 3.1b, c). XRD spectra collected for both samples confirmed that the akaganeite nanowires are completely converted into hematite (JCPDS 33-0664) (Figure 3.2). The strongest (110) diffraction peak indicates that these hematite nanowire arrays have a preferred

[110] direction on the substrate, which implies that they were grown along [110] axis. It has been reported that the conductivity of hematite along [110] direction is four orders of magnitude higher [001] direction due to a hopping mechanism related with $\text{Fe}^{2+}/\text{Fe}^{3+}$ mixed valence states.²⁶

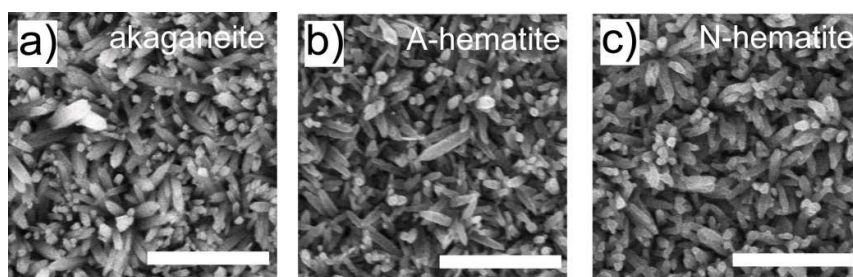


Figure 3.1 SEM images of akaganeite nanowire arrays (a), hematite nanowire arrays annealed in air (b) and $\text{N}_2 + \text{air}$ (c) at 550 °C. Scale bars are 1 μm.

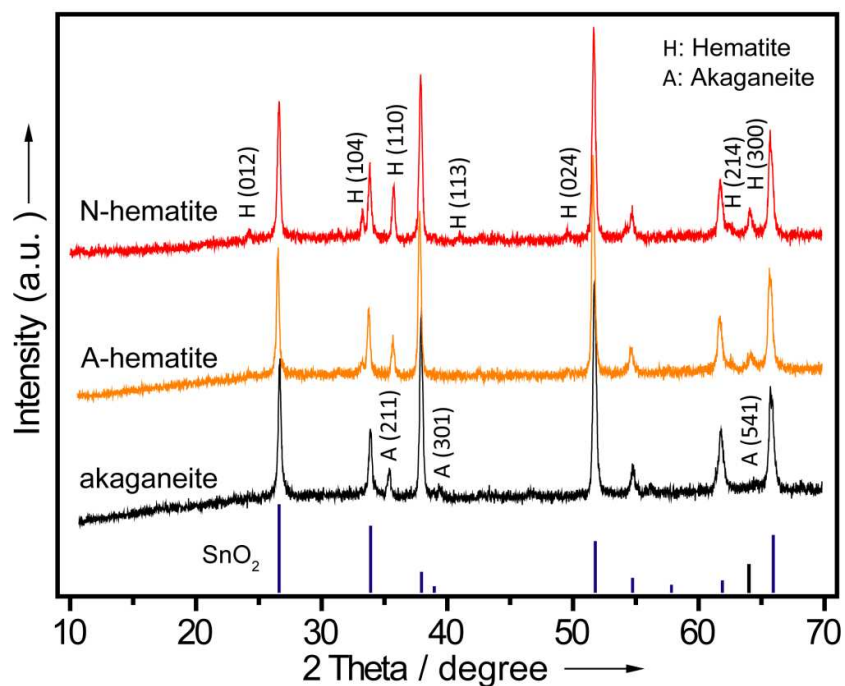


Figure 3.2 Corresponding XRD spectra collected for akaganeite and hematite samples. Diffraction peaks for hematite (JCPDS 33-0664) and akaganeite

(JCPDS 75-1594) are labeled with H(hkl) and A(hkl), respectively. The lines at bottom highlight the diffraction peaks of SnO₂ (JCPDS 41-1445) from FTO substrate.

PEC performance of these hematite photoanodes were measured in an electrochemical cell with a coiled Pt wire counter electrode and an Ag/AgCl reference electrode, using 1 M NaOH pH 13.6 electrolyte deaerated by purging N₂ gas. The measured potentials vs. Ag/AgCl are converted to reversible hydrogen electrode (RHE) scale according to the Nernst equation,

$$E_{\text{RHE}} = E_{\text{Ag/AgCl}} + 0.059 \text{ pH} + E_{\text{Ag/AgCl}}^{\circ}$$

where E_{RHE} is the converted potential vs. RHE, $E_{\text{Ag/AgCl}}^{\circ} = 0.1976 \text{ V}$ at 25 °C, and $E_{\text{Ag/AgCl}}$ is the experimentally measured potential against Ag/AgCl reference electrode. As shown in Figure 3.3, A-hematite sample (prepared in air) yields a minimal photocurrent density in the potential range we studied under 100 mW/cm² illumination. It is consistent with previous results reported by our group and others, in which a high temperature between 650 and 800 °C is typically required for activating these hematite samples to achieve reasonable photoactivity.^{2, 19, 29} In contrast, the N-hematite sample (prepared in N₂ + air) shows pronounced photoactivity. It yields a photocurrent density of 1.82 mA/cm² at 1.23 V vs. RHE, and achieved a maximum value of 3.37 mA/cm² at 1.50 V vs. RHE (Figure 3.3). To our knowledge, this is the best photocurrent density ever achieved by undoped hematite nanowire-based photoanode.

Furthermore, we have performed amperometric $I-t$ studies, at an applied voltage of 1.5 V vs. RHE at 100 mW/cm^2 , to examine the photoresponse of N-hematite over time. The photocurrent density of N-hematite is stable in NaOH electrolyte solution (pH=13.6) at least for one hour. The onset potential is about 1.0 V vs. RHE, which is similar to other hematite photoanodes sintered at similar temperature without oxygen-evolving catalysts.^{4, 30} The on-set potential of N-hematite dark current is slightly shifted to higher potential could be due to the increased overpotential as a result of increased oxygen vacancies (Fe^{2+} sites) on the surface of N-hematite photoanode compared to that of A-hematite. It has been reported that Fe^{2+} sites serve as recombination centers for photoexcited holes, which could increase the overpotential for water oxidation.^{31,32}

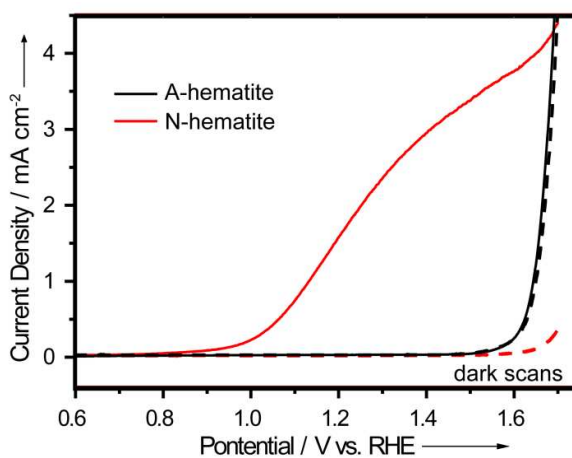


Figure 3.3 Linear sweep voltammograms collected for A-hematite (black lines) and N-hematite (red lines), at a scan rate of 10 mV/s, in 1 M NaOH electrolyte (pH 13.6) under illumination of simulated solar light of 100 mW/cm^2 (solid lines) and in the dark (dashed lines).

Incident-photon-to-current-conversion-efficiencies (IPCE) collected for hematite photoanodes as a function of wavelength under bias at 1.23 and 1.50 V vs. RHE are shown in Figure 3.4. IPCE were calculated from the photocurrent densities obtained under different wavelengths in a range from 320 to 650 nm, and expressed as the following equation:

$$\text{IPCE} = (1240 I) / (\lambda J_{\text{light}})$$

where I (mA/cm²) is the photocurrent density, λ (nm) is the incident wavelength, and J_{light} (mW/cm²) is the power density of irradiance at a specific wavelength. The IPCE for A-hematite measured at 1.50 V vs. RHE is 0.57 % at 390 nm, which is consistent with its minimal photocurrent. The N-hematite shows significantly enhanced IPCE values over the entire wavelengths (320 to 650 nm). The sample yields maximum IPCE values of 26 % and 64 % at 360 nm, measured at 1.23 V and 1.50 V vs. RHE, respectively. IPCE values gradually drop to zero at the wavelength above 610 nm, in accordance with the bandgap of hematite. To verify and correct the possible discrepancy in incident light profile between our xenon lamp setup and the standard global solar light (AM 1.5G, 100 mW/cm²), we integrate the IPCE spectra of N-hematite with a standard AM 1.5G spectral irradiance (ASTM G-173-03). The photocurrent density measured at 1.5 V vs. RHE was calculated according to the following equation:

$$I_{1.50\text{V vs RHE}} = \int_{320}^{650} \text{IPCE}(\lambda) E(\lambda) d\lambda = 3.1 \text{ mA/cm}^2$$

where $E(\lambda)$ is the solar spectral irradiance at a specific wavelength (λ), and $IPCE(\lambda)$ is the obtained IPCE profile of hematite sample as a function of wavelengths (λ) at 1.50 V vs. RHE. The calculated photocurrent, 3.11 mA/cm², is only slightly smaller than the value of 3.37 mA/cm² obtained experimentally in PEC measurement (Figure 3.3) at 1.50 V vs. RHE. It shows that the discrepancy due to the mismatch between the simulated light used in the PEC experiments and the standard AM 1.5G solar spectrum is minor. Importantly, the PEC results unambiguously show that thermal activation of akaganeite nanowire arrays in an oxygen-deficient atmosphere (N₂ + air) at 550 °C is a simple and effective strategy to prepare high performance hematite for water oxidation.

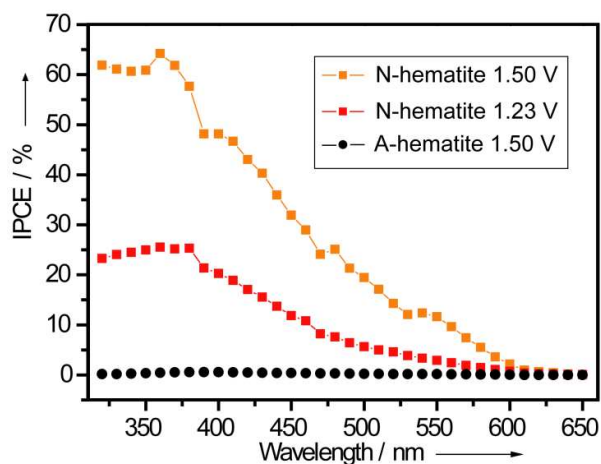


Figure 3.4 Corresponding IPCE spectra for A-hematite (dot/line) and N-hematite (square/line), collected at potentials of 1.23 and 1.50 V vs. RHE.

The understanding of mechanism in enhancing photoactivity is important for design and fabrication of hematite photoanode. Structural analysis confirms

that there is no obvious difference in morphology or crystal phase for hematite nanowires prepared in two environments (Figure 3.1). The enhanced photocurrent in N-hematite (compared to A-hematite) is believed to be due to the improved conductivity as a result of the creation of V_o by annealing the sample in an oxygen-deficient atmosphere. V_o is known to be a shallow donor for hematite.³ To investigate the carrier densities of hematite samples, their electrochemical impedance were measured at 10 kHz frequency in the dark. Mott-Schottky plots are generated based on the capacitances derived from the electrochemical impedance obtained at each potential (Figure 3.5), in which the flatband potential (V_{FB}) and the donor density (N_d) can be estimated. The V_{FB} for A-hematite and N-hematite are found to be 0.41 and 0.36 V vs. RHE, which are consistent with literature reported values for hematite.²⁵ Their N_d can be determined from the Mott-Schottky equation

$$N_d = (2/e_0\epsilon\epsilon_0)[d(1/C^2)dV]^{-1}$$

where e_0 is the electron charge (1.602×10^{-19} C), ϵ is the dielectric constant of hematite (80),¹⁸ ϵ_0 is the permittivity of vacuum (8.854×10^{-12} F m⁻¹), C is the capacitance derived from the electrochemical impedance obtained at each potential (V) with 10 kHz frequency in the dark. The donor density of the N-hematite was calculated to be 3.65×10^{20} cm⁻³, which is an order of magnitude higher than that of A-hematite (3.34×10^{19} cm⁻³). The increased donor density improves the conductivity, and thereby the collection efficiency of photoexcited

electrons.

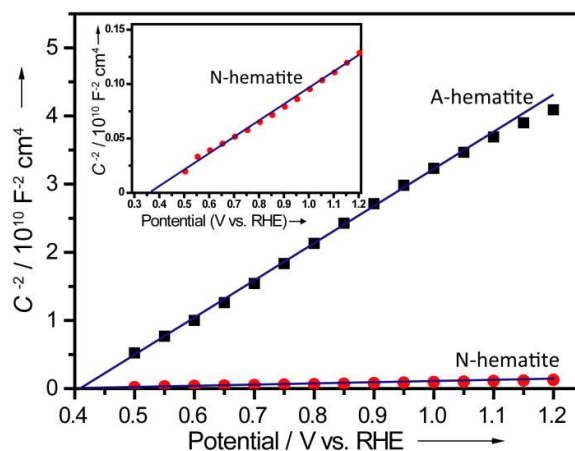


Figure 3.5 Mott-Schottky plots measured for A-hematite (squares) and N-hematite (circles) nanowire films. The x-intercepts of the linear fitting best-fit lines were used to estimate the flatband potential (V_{FB}). Inset: magnified Mott-Schottky plot of N-hematite.

While the synthetic method of N-hematite does not involve dopant, the enhanced donor density is expected to be due to the creation of V_{o} during thermal activation in oxygen-deficient environment. To verify this hypothesis, we measured Fe 2p core-level X-ray photoelectron spectroscopy (XPS) spectra for N- and A-hematite as well as their difference spectrum (Figure 3.6). The Fe $2p_{3/2}$ peaks of both samples are centered at the binding energies of ~ 711.4 eV, which is typical value observed for Fe^{3+} in Fe_2O_3 and Fe_3O_4 .³³⁻³⁵ The binding energy is not compatible with that of FeO .³⁶ A satellite peak of the Fe $2p_{3/2}$ main line is observed in both samples at approximately 719 eV. This satellite is most likely indicative of the presence of Fe^{3+} species.²⁹ Importantly, there is no

evidence to support the presence of Fe^{2+} in A-hematite, which should give rise to a satellite peak located at 716 eV.³³ In contrast, N-hematite sample exhibits an obvious satellite peak around 716 eV corresponding to Fe^{2+} ³³ (Figure 3.6). The results suggest that Fe^{2+} sites (V_o) were created in N-hematite. $\text{Fe}^{2+}(\text{V}_\text{o})$ act as a shallow donor and therefore increase the donor density of hematite,³⁷ which is supported by the Mott-Schottky analysis. Furthermore, valence band spectra of A- and N-hematite were measured by Mg $\text{K}\alpha$ XPS. An estimate of the valence band maximum by linear extrapolation to the baseline derives band edge positions of ~ 1.60 eV and ~ 1.50 eV below the Fermi energy for N-hematite and A-hematite samples, respectively. The fact that N-hematite sample exhibit slightly increased band edge position (compared to A-hematite) indicates an increase of donor density. This result again supports the hypothesis of increased donor density by creating oxygen vacancy state and consistent with the results of Mott-Schottky studies.

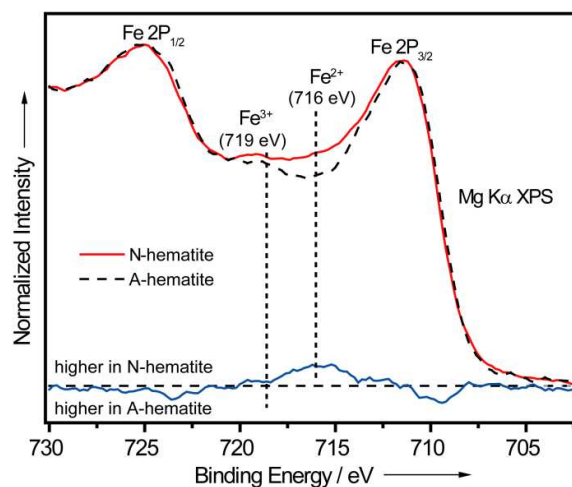
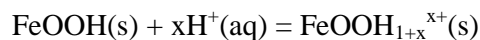


Figure 3.6 Overlay of Fe 2p XPS spectra of A-hematite (black dashed curve) and N-hematite (red solid curve) films, together with their difference spectrum (“N-hematite” minus “A-hematite”). The dashed lines highlight the satellite peaks for Fe³⁺ and Fe²⁺.

We managed to investigate the mechanism and the influence of oxygen content in thermal treatment on the creation of V_o, and eventually to control the donor density of hematite. The thermal decomposition of akaganeite to hematite is a critical step, which can be described as the following equation

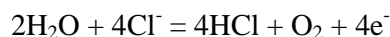


β-FeOOH is a three-dimensional tunnel structure,³⁸ which was commonly formed via hydrolysis of FeCl₃ in an acidic (pH 1.5) environment. It has been reported that the as-prepared β-FeOOH typically contains chloride ions (Cl⁻) and protons (H⁺) in the inner space of tunnels.^{39,40} In an acidic medium, β-FeOOH will uptake protons from solution as illustrated in following equation³⁹

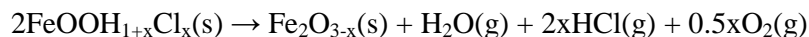


To balance the charge, a stoichiometric amount of chloride ions will be captured by the crystal at the same time. Then the chemical formula of akaganeite can be expressed as FeOOH_{1+x}Cl_x. The chloride concentration (x value) varies based on the crystal size and synthetic conditions, such as pH value.³⁹⁻⁴¹ It has been reported that the captured chloride ions can be released in a form of hydrogen chloride by reaction with the water molecules produced by dehydroxylation upon thermal treatment on or above 200 °C, producing oxygen

as a side-product as shown in the following equation.^{38, 39}



The oxygen-deficiency environment could facilitate the release of hydrogen chloride by shifting the reaction balance to the right hand side. We anticipate that the released electrons were used to reduce Fe^{3+} to Fe^{2+} . Therefore, the thermal decomposition of chloride-contained akaganeite in N_2 atmosphere can be described as



whereas the O_2 molecule are formed as the result of dehydroxylation of $\beta\text{-FeOOH}$ and removed by the N_2 gas flow. The formation of $\text{Fe}_2\text{O}_{3-x}$ species with V_o and dual-oxidation states ($\text{Fe}^{2+}/\text{Fe}^{3+}$) supported by the XPS and Mott-Schottky analysis. In contrast, an oxygen-rich atmosphere, such as air, hinders the release of hydrogen chloride, and akaganeite could completely convert into $\alpha\text{-Fe}_2\text{O}_3$ by forming chlorine (Cl_2) through chloride oxidation by oxygen.



Based on the above hypothesis, there are two major parameters in controlling the creation of V_o in hematite: the oxygen content during thermal treatment and the presence of chloride ions. To confirm this hypothesis, we carried out the thermal decomposition of akaganeite at 550 °C for 2 hr in three different environments: oxygen-rich (air), oxygen-deficient (N_2 + air) and zero-oxygen (high-purity N_2) atmosphere. Note that the oxygen-rich and

deficient environments are the same conditions used for preparing A- and N-hematite samples. To create zero-oxygen environment, the tube furnace was vacuumed to a pressure <20 mTorr and then refilled with N_2 . This vacuum-fill process was repeated for at least three times to ensure no/minimal residual air in the tube. Akaganeite samples thermally treated in various environments lead to films with different colors (Figure 3.7). The A- and N-hematite samples are red, while the sample prepared in zero-oxygen environment is black. Raman spectra of the two red samples (Figure 3.8a) can be indexed to the six characteristic Raman peaks of hematite in the range of $200-800\text{ cm}^{-1}$.⁴² Noteworthy that the intensity of characteristic Raman peaks for hematite are completely disappeared in the black sample obtained in high purity N_2 atmosphere. XRD analysis confirms the black sample is magnetite (Fe_3O_4) (Figure 3.8b). Akaganeite-to-magnetite conversion has been observed in the thermal decomposition of akaganeite in vacuum.⁴³ To investigate the role of captured chloride ion in the thermal decomposition of FeOOH into hematite, we prepared FeOOH without chloride ion as a negative control. FeOOH without chloride was synthesized in the same conditions but replacing $FeCl_3$ precursor solution with $Fe(NO_3)_3$ solution. The pH value (1.5) is adjusted by HNO_3 instead of HCl solution as well. FeOOH samples prepared with $FeCl_3$ or $Fe(NO_3)_3$ precursor solutions thermal treated at $550\text{ }^\circ\text{C}$ for 2 hr in high-purity N_2 atmosphere showed distinct results. The sample without chloride is orange instead of black

in color after thermal treatment (Figure 3.7), and it is confirmed to be hematite by Raman spectroscopy (Figure 3.8a). To further confirm the effect of chloride ions in the thermal decomposition of akaganeite, we have carried out additional experiment. The as-prepared akaganeite samples were put into 0.5 M or 1M NaOH solution at 55 °C for 3 hr to exchange the Cl⁻ anion with OH⁻.³⁹ A control experiment by soaking akaganeite into deionized water at 55 °C for 3 hr was carried out in parallel. We thermally treated both anion-exchanged and control samples at 550 °C in zero-oxygen atmosphere with continuous high-purity N₂ gas flow. The samples show different colors after thermal annealing. As expected the control sample turned black, which indicates the formation of magnetite. In contrast, the anion-exchanged samples (with 0.5 M or 1 M NaOH) are red, which is the typical color for hematite. This experiment again confirms that Cl⁻ anion remaining in the structure of akaganeite is essential for the creation of Fe²⁺ sites (Vo), and supports the proposed akaganeite-magnetite transformation mechanism.









	as-prepared FeOOH	Thermal decomposition of akaganeite in		
		air	N ₂ +air	N ₂
a) typical system				
b) No-Cl system				

Figure 3.7 Summary of digital pictures of FeOOH prepared in (a) typical

system (with Cl^-) and (b) No-Cl system (without Cl^-); and the products of thermal decomposition of akaganeite in three different environments: oxygen-rich (air), oxygen-deficient ($\text{N}_2 + \text{air}$) and zero-oxygen (high-purity N_2) atmosphere.

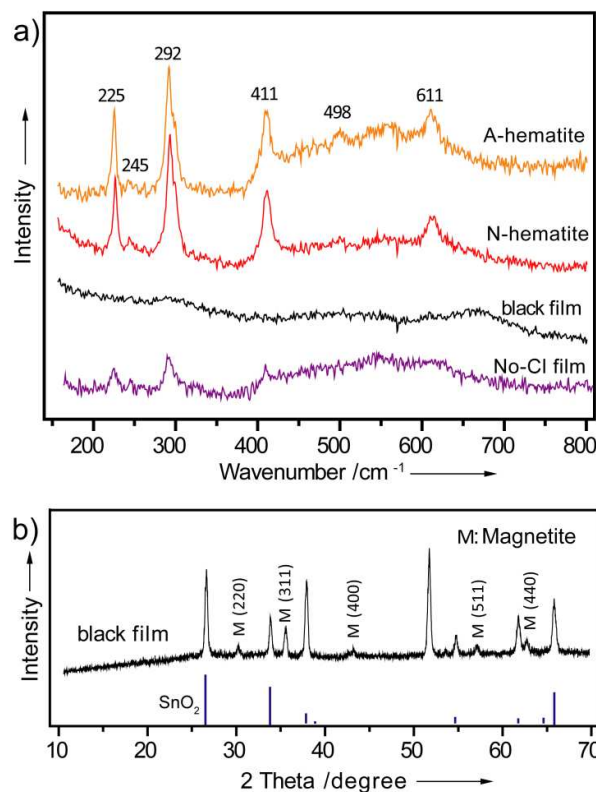


Figure 3.8 (a) Raman spectra of akaganeite samples thermally treated in air (A-hematite), oxygen-deficient ($\text{N}_2 + \text{air}$; N-hematite) and N_2 environments (black film). The akaganeite sample, prepared by $\text{Fe}(\text{NO}_3)_3$ precursor solution, thermally treated in N_2 (No-Cl film). (b) XRD spectrum collected for the akaganeite samples thermally treated in N_2 at $550\text{ }^\circ\text{C}$. Diffraction peaks labeled with $\text{M}(\text{hkl})$ can be indexed to magnetite (JCPDS 19-0629). The lines at bottom highlight the diffraction peaks of SnO_2 (JCPDS 41-1445) from FTO substrate.

3.4 Conclusion

To summarize, thermal treatment of akaganeite nanowire arrays in an oxygen-deficient environment at $550\text{ }^\circ\text{C}$ achieved significantly improved

photoactivity for water oxidation, compared to the samples that thermally activated in air. The hematite nanowire-arrayed photoanode yields a photocurrent density of 3.37 mA/cm^2 at 1.50 V vs. RHE , which is the best value reported for pristine hematite materials without the incorporation of dopants or oxygen-evolving catalysts. The enhancement in photoactivity is due to the increased donor density as a result of the formation of $V_o (\text{Fe}^{2+})$. The presence of chloride ions and an oxygen-deficient environment are essential for the creation of V_o . This work demonstrated a simple and effective strategy for the preparation of highly photoactive hematite for PEC water oxidation, without the need of dopants and at a relatively low activation temperature.

References

1. H. L. Wang, J. A. Turner, *J. Electrochem. Soc.* **2010**, 157, F173.
2. Y. Ling, G. Wang, D. A. Wheeler, J. Z. Zhang, Y. Li, *Nano Lett.* **2011**, 11, 2119.
3. K. Sivula, F. Le Formal, M. Grätzel, *ChemSusChem* **2011**, 4, 432.
4. S. D. Tilley, M. Cornuz, K. Sivula, M. Grätzel, *Angew. Chem. Int. Ed.* **2010**, 49, 6405.
5. Y. Lin, Z. S., S. W. Sheehan, D. Wang, *J. Am. Chem. Soc.* **2011**, 133, 2398.
6. G. Wang, H. Wang, Y. Ling, Y. Tang, X. Yang, R. C. Fitzmorris, C. Wang, J. Z. Zhang, Y. Li, *Nano Lett.* **2011**, 11, 3026.

7. A. Fujishima, K. Honda, *Nature* **1972**, 238, 37.
8. Y. Lin, S. Zhou, X. Liu, S. Sheehan, D. Wang, *J. Am. Chem. Soc.* **2009**, 131, 2772.
9. Y. J. Hwang, A. Boukai, P. Yang, *Nano Lett.* **2008**, 9, 410.
10. X. Feng, K. Shankar, O. K. Varghese, M. Paulose, T. J. Latempa, C. A. Grimes, *Nano Lett.* **2008**, 8, 3781.
11. G. M. Wang, X. Y. Yang, F. Qian, J. Z. Zhang, Y. Li, *Nano Lett.* **2010**, 10, 1088.
12. R. Solarska, A. Krolikowska, J. Augustynski, *Angew. Chem. Int. Ed.* **2011**, 49, 7980.
13. J. Z. Su, X. J. Feng, J. D. Sloppy, L. J. Guo, C. A. Grimes, *Nano Lett.* **2011**, 11, 203.
14. J. Z. Su, L. J. Guo, N. Z. Bao, C. A. Grimes, *Nano Lett.* **2011**, 11, 1928.
15. R. Liu, Y. Lin, L.-Y. Chou, S. W. Sheehan, W. He, F. Zhang, H. J. M. Hou, D. Wang, *Angew. Chem. Int. Ed.* **2011**, 50, 499.
16. N. J. Cherepy, D. B. Liston, J. A. Lovejoy, H. M. Deng, J. Z. Zhang, *J. Phys. Chem. B* **1998**, 102, 770.
17. M. P. Dareedwards, J. B. Goodenough, A. Hamnett, P. R. Trellick, *J. Chem. Soc. Faraday Trans.* **1983**, 79, 2027.
18. I. Cesar, K. Sivula, A. Kay, R. Zboril, M. Graetzel, *J. Phys. Chem. C* **2009**, 113, 772.

19. K. Sivula, R. Zboril, F. Le Formal, R. Robert, A. Weidenkaff, J. Tucek, J. Frydrych, M. Grätzel, *J. Am. Chem. Soc.* **2010**, 132, 7436.
20. M. G. Walter, E. L. Warren, J. R. McKone, S. W. Boettcher, Q. X. Mi, E. A. Santori, N. S. Lewis, *Chem. Rev.* **2010**, 110, 6446.
21. D. K. Zhong, M. Cornuz, K. Sivula, M. Grätzel, D. R. Gamelin, *Energy Environ. Sci.* **2011**, 4, 1759.
22. D. K. Zhong, D. R. Gamelin, *J. Am. Chem. Soc.* **2010**, 132, 4202.
23. D. K. Zhong, J. W. Sun, H. Inumaru, D. R. Gamelin, *J. Am. Chem. Soc.* **2009**, 131, 6086.
24. J. Brilliet, M. Grätzel, K. Sivula, *Nano Lett.* **2010**, 10, 4155.
25. M. Zhang, W. Luo, Z. Li, T. Yu, Z. Zou, *Appl. Phys. Lett.* **2010**, 97, 042105.
26. N. Iordanova, M. Dupuis, K. M. Rosso, *J. Chem. Phys.* **2005**, 122, 144305.
27. C. Castro, L. Oliveira, M. Guerreiro, *Catal. Lett.* **2009**, 133, 41.
28. L. Vayssieres, N. Beermann, S. E. Lindquist, A. Hagfeldt, *Chem. Mater.* **2001**, 13, 233.
29. R. Morrish, M. Rahman, J. M. D. MacElroy, C. A. Wolden, *ChemSusChem* **2011**, 4, 474.
30. A. Kay, I. Cesar, M. Grätzel, *J. Am. Chem. Soc.* **2006**, 128, 15714.
31. A. Duret, M. Grätzel, *J. Phys. Chem. B* **2005**, 109, 17184.

32. R. van de Krol, M. Grätzel, Springer, New York Dordrecht Heidelberg London, **2011**, pp. 147.
33. T. Fujii, F. M. F. de Groot, G. A. Sawatzky, F. C. Voogt, T. Hibma, K. Okada, *Phys. Rev. B* **1999**, 59, 3195.
34. G. Wang, Y. Ling, D. A. Wheeler, K. E. N. George, K. Horsley, C. Heske, J. Z. Zhang, Y. Li, *Nano Lett.* **2011**, 11, 3503.
35. K. Wandelt, *Surf. Sci. Rep.* **1982**, 2, 1.
36. J. F. Moulder, W. F. Stickle, In Physical Electronics Division, Perkin-Elmer Coporation, Eden Prairie, MN, **1992**.
37. V. M. Aroutiounian, V. M. Arakelyan, G. E. Shahnazaryan, H. R. Hovhannisyan, H. Wang, J. A. Turner, *Solar Energy* **2007**, 81, 1369.
38. E. Paterson, R. Swaffield, D. R. Clark, *Thermochim. Acta* **1982**, 54, 201.
39. J. Cai, J. Liu, Z. Gao, A. Navrotsky, S. L. Suib, *Chem. Mater.* **2001**, 13, 4595.
40. K. Stahl, K. Nielsen, J. Jiang, B. Lebech, J. C. Hanson, P. Norby, J. van Lanschot, *Corrosion Science* **2003**, 45, 2563.
41. K. M. Parida, *J. Mater. Science* **1988**, 23, 1201.
42. D. L. A. de Faria, S. Venâncio Silva, M. T. de Oliveira, *J. Raman Spectrosc.* **1997**, 28, 873.
43. M. D. Merono, J. Morales, J. L. Tirado, *Thermochim. Acta* **1985**, 92, 525.

Chapter 4

Low Temperature Activation of Hematite Nanowires for Photoelectrochemical Water Oxidation

Abstract

Hematite (α -Fe₂O₃) nanostructures have been extensively studied as photoanode material for photoelectrochemical (PEC) water oxidation. However, the photoactivity of pristine hematite nanostructures are fairly low and typically requires thermal activation at temperature of 650 °C or above. Here we report a new method for enhancing the photocurrent of hematite nanowires at substantially lower temperature of 350 °C via a two-step annealing process (activation process). Hydrothermally grown β -FeOOH nanowires were first annealed in pure N₂ environment at 350 °C to form magnetite, followed by partial oxidation in air to convert magnetite to hematite. During this process, Fe²⁺ sites (oxygen vacancies) were intentionally created to increase the donor density and therefore the electrical conductivity of hematite. The oxygen-deficient hematite nanowire photoanode created at low temperature (350 °C) show considerably enhanced photoactivity compared to pristine hematite sample that prepared by thermal annealing of β -FeOOH nanowires at 550 °C in

air. Moreover, this low temperature annealing method can be coupled with element doping method to further increase the photoactivity of hematite nanowire. Sn-doped hematite nanowires prepared by the same low temperature annealing method show at least three fold enhanced photocurrent compared to the undoped sample. Significantly, the highest temperature in the entire annealing process was 350 °C, which is the lowest activation temperature ever reported for hematite nanowire photoanodes.

4.1 Introduction

Hematite ($\alpha\text{-Fe}_2\text{O}_3$) is a promising photoanode material for PEC water oxidation because of its favorable band-gap of 2.1 eV.¹⁻⁴ However, hematite also has several key limitations, including poor electrical conductivity,⁵⁻¹¹ short excited state lifetime,^{3,12} slow oxygen evolution reaction kinetics,¹³⁻¹⁶ and short diffusion length for holes.¹⁷⁻¹⁹ The recent development of hematite nanowire photoanode holds great promise for addressing some of these limitations.^{6,7,20} For instance, nanowires provide considerably larger surface area for water oxidation compared to bulk material.²⁰⁻²² The high aspect ratio of nanowire structure not only enables efficient light absorption along the nanowire growth axis, but also offer substantially reduced distance for photogenerated holes diffusing to the semiconductor/electrolyte interface.¹ A number of methods have been reported to synthesize high-density hematite nanowires on conductive

substrates.^{20,23-29} Among them, hydrothermal synthesis is one of the most simple, low-cost, and scalable growth approach.¹⁹ However, the photoactivity of hydrothermally grown pristine hematite nanowires are fairly low and typically requires thermal activation at temperature of 650 °C or above. In previous reports, the thermal activation has been used to facilitate the incorporation of substitutional dopants into hematite^{6,20,30-33} and/or improve the optical properties of hematite.^{34,35} Furthermore, Warren and co-workers showed that the presence of grain boundaries in polycrystalline hematite nanostructures limits their incident photon-to-current efficiency. Thermal annealing can reorient adjacent grains of hematite and passivate grain boundaries to facilitate the electronic transport among hematite network.⁸ Yet, this high temperature activation step is an energy intensive process and would certainly increase the cost of device fabrication, which is not favorable for practical application. Additionally, the high temperature treatment can damage the growth substrate (*e.g.*, transparent conductive oxide coated glass substrate).⁶ Thus, to activate hematite photoanode at low temperature is highly desirable.

Recently, we have demonstrated that highly photo-active hematite nanowire photoanode can be produced by annealing the β -FeOOH nanowires in an oxygen-deficient environment at 550 °C.⁷ The enhanced performance was attributed to the increased donor density of hematite electrode as a result of formation of Fe^{2+} (oxygen vacancy), which serve as a shallow donor for

hematite.^{7,36} The increased electron density could improve charge separation at the semiconductor/electrolyte interface, reduce the energy loss due to IR drop in the semiconductor, and decrease the contact resistance at the semiconductor/FTO interface. The capability of increasing the charge transfer efficiency of hematite through controlled creation of oxygen vacancies indeed opens up a new opportunity to “activate” hematite materials at lower temperature. In this study, we demonstrate that the photoactivity of hydrothermally grown hematite nanowires can be improved at as low as 350 °C by creation of oxygen vacancies. To our knowledge, this is the lowest activation temperature ever reported for hematite nanowire photoanode.

4.2 Experimental Section

Hematite nanowire arrays growth:

Hematite nanowire arrays were fabricated on a FTO coated glass substrate (TEC 8, Hartford Glass Company Inc.) based on a previously reported method.⁶ A Teflon-lined stainless steel autoclave of 30 mL capacity was filled with 20 mL aqueous solution containing 0.15 M of ferric chloride ($\text{FeCl}_3 \cdot 6\text{H}_2\text{O}$, Acros, 99+%) and 1 M sodium nitrate (NaNO_3 , Fisher 99.4%) at pH 1.5 (adjusted by HCl). A piece of FTO substrate, washed with acetone, ethanol, and then deionized water, was put into the autoclave and heated in an oven at 95 °C for 4 hr and then let it naturally cool down to ambient temperature. A uniform yellow

layer of akaganeite nanowire film was obtained on the FTO substrate. The akaganeite-coated substrate was then washed with deionized water and blown dry with air. Nitrogen treated samples were annealed in N₂ atmosphere in a tube furnace. The tube furnace was first vacuumed to a pressure of 15 mTorr, and then filled with ultrahigh purity N₂ (99.998%, Praxair) to 100 Torr. This process has been repeated for 3 times. The sintering was carried out at temperatures between 200 and 425 °C for 1 hr at 740 Torr pressure with a N₂ flow rate of 50 standard cubic centimeters per minute (sccm). To convert magnetite to hematite, the black samples were annealed on a hot plate in air at 350 °C for 30 min.

Material characterization:

Scanning electron microscopy (SEM) images were collected with a field-emission SEM (Hitachi S-4800II). Transmission electron microscopy (TEM) images were collected in a FEI Monochomated F20 UT Technai TEM/STEM operated at 200 kV. X-ray diffraction (XRD) spectra were collected with a Rigaku Americas Miniflex Plus powder diffractometer. Diffraction spectra were recorded from a two-theta angle of 20 to 70 degree with a step size of 0.04 degree at a rate of 1 degree/min. Raman spectroscopy measurements were carried out on a Nicolet Almega XR Dispersive Raman spectrometer (laser wavelength 780 nm). X-ray photoelectron Spectroscopy (XPS) was performed on a RBD upgraded PHI-5000C ESCA system (Perkin-Elmer) using Mg-monochromatic X-ray at a power of 25 W with an X-ray-beam diameter of

10 mm, and a pass energy of 29.35 eV. The pressure of analyzer chamber was maintained below 5×10^{-8} Pa during the measurement. The binding energy was calibrated using the C 1s photoelectron peak at 284.6 eV as reference.

Photoelectrochemical measurement:

PEC measurements were carried out in a three-electrode electrochemical cell using hematite nanowire sample as working electrode, a coiled Pt wire as counter electrode and an Ag/AgCl electrode as reference electrode. An aqueous solution of 1 M NaOH with a pH 13.6 was used as the electrolyte, deaerated by purging N₂ gas into electrolyte. The substrate was sealed on all edges with epoxy resin except for an average working area of 0.20 cm². All linear sweep voltammograms were measured by a CHI 660D electrochemical workstation (CH instruments, Inc., Austin, TX), with front side illumination using a solar simulator (Newport 69920, 1000 W xenon lamp) coupled with an infrared water filter (Oriel 6127) and an AM 1.5 global filter (Newport 81094). The power density of 100 mW/cm² was measured with a power meter (Molelectron, PM5100). Incident-photo-to-current-efficiencies (IPCE) were measured with the same xenon lamp coupled with a monochromator (Oriel Cornerstone 130 1/8m). EIS measurements were carried out in the same electrochemical setup as PEC measurement. A potential varying from 0 to 0.4 V vs. Ag/AgCl was applied, and the system was allowed to equilibrate for 5 min. An alternating-current perturbation of the applied potential (with a magnitude of 5 mV and frequencies

changing from 100 kHz to 1 Hz) was then exerted, and the impedance changes in response to the perturbation were measured.

4.3 Results and Discussion

Hematite nanowires were prepared on fluorine-doped tin oxide (FTO) glass substrate by a two-step growth process. Figure 4.1a illustrates the first growth step, in which β -FeOOH nanowire arrays were synthesized on a FTO substrate through the hydrolysis of 0.15 M FeCl₃ in an aqueous solution with a high ionic strength (1M NaNO₃) and low pH value (pH 1.5, adjusted by HCl) at 95 °C for 4 hr.^{7,26} The as-prepared yellow film of β -FeOOH was further annealed in pure N₂ atmosphere to introduce oxygen vacancies. To study the temperature effect, β -FeOOH films were annealed at four different temperatures (200, 300, 350, and 425 °C) in pure N₂ atmosphere for 1 hr. Samples are denoted as “N-Temperature”, i.e. N200 refers to the β -FeOOH sample annealed at 200 °C in N₂. Upon thermal annealing, obvious color changes of yellow β -FeOOH films were observed. As shown in Figure 4.1b, the colour of samples N200 and N300 are red, while samples N350 and N425 are black. Scanning electron microscopy (SEM) analysis revealed that there was no obvious morphology difference among these samples (Figure 4.1c). These results suggested the N300 and N350 samples could have different crystal structures. A phase change occurred at the temperature between 300 and 350 °C.

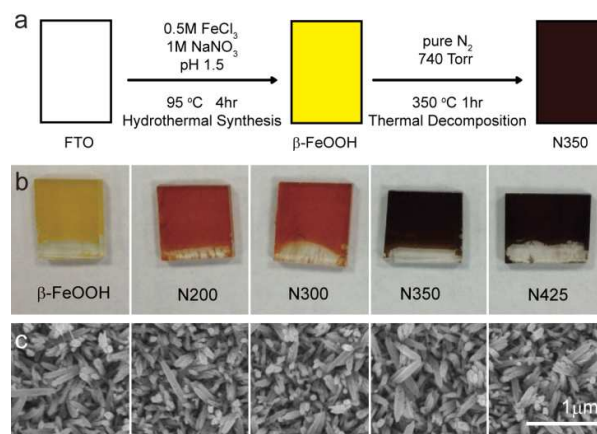


Figure 4.1 (a) A scheme illustration of the preparation of β -FeOOH nanowire arrays on FTO substrate, followed by the thermal decomposition of β -FeOOH in pure nitrogen at 350 °C. (b) Digital pictures and (c) SEM images of β -FeOOH and its thermal decomposition products obtained at different temperatures between 200 and 425 °C in a pure N_2 environment.

X-ray diffraction (XRD) and Raman spectroscopy measurements were carried out to characterize these nitrogen-annealed β -FeOOH samples (Figure 4.2). XRD studies revealed that the two red films, N200 and N300, exhibit characteristic diffraction peaks of hematite (α - Fe_2O_3 ; JCPDS 33-0664), while the black films, N350 and N425, contained characteristic diffraction peaks of magnetite (Fe_3O_4 ; JCPDS 19-0629).

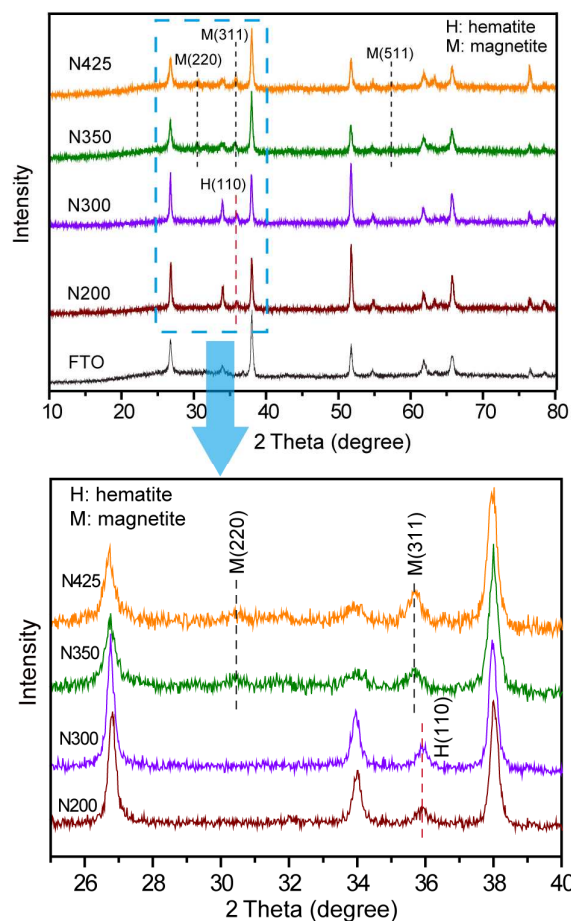


Figure 4.2 XRD spectra collected for N200, N300, N350, N425 samples, and FTO substrate. Diffraction peaks for hematite (JCPDS 33-0664) and magnetite (JCPDS 19-0629) are labelled with H(hkl), and M(hkl), respectively.

N200 and N300 exhibited six characteristic Raman peaks of hematite in the wavenumber range between 200 and 800 cm^{-1} (Figure 4.3). Raman spectra of N350 and N425 showed three broad peaks around 300, 500, and 663 cm^{-1} that can be indexed to the characteristic peaks of magnetite.³⁷ The XRD and Raman spectroscopy results elucidate the phase transitions from akaganeite to hematite, and then magnetite in nitrogen atmosphere (oxygen deficient environment) as

the increase of annealing temperature. In contrast, hematite is the only product of thermal annealing of akaganeite in air in the same range of temperatures.

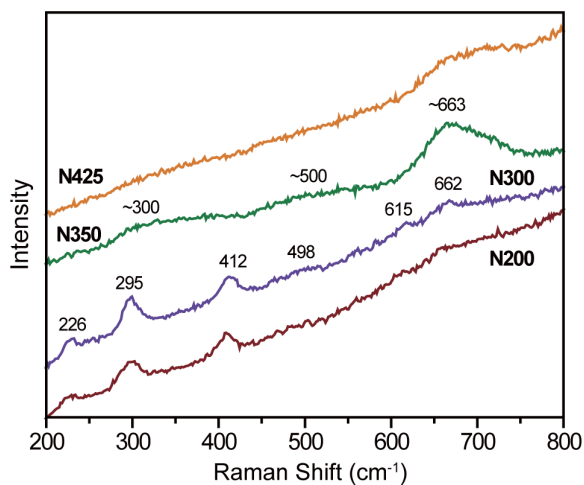
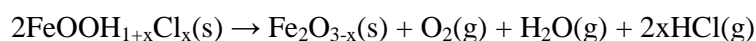


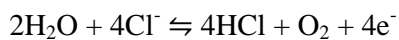
Figure 4.3 Raman spectra of N200, N300, N350, and N425 samples.

The previous study has demonstrated that the formation of magnetite is related to the oxygen content during the annealing process as well as the presence of adsorbed chloride ions in akaganeite.⁷ The thermal decomposition of chloride-containing akaganeite in a N₂ atmosphere can be described by the following equation:



where FeOOH_{1+x}Cl_x represents akaganeite with adsorbed chloride ions because FeCl₃ was used as Fe precursor for the growth of FeOOH nanowires. The creation of oxygen deficient iron oxide (Fe₂O_{3-x}) could be attributed to the partial reduction of Fe³⁺ site by the electrons created from the following redox

reaction^{7,38}:



in which adsorbed water and chloride ions react to form hydrogen chloride, oxygen and electrons. With sufficient supply of oxygen, the forward reaction is not favorable. Yet, in an oxygen-deficient environment, the reaction will shift to favor the formation of oxygen and create electrons for reduction of Fe^{3+} . The reaction is expected to be an uphill reaction that requires activation energy. The formation of magnetite (with large amount of Fe^{2+} sites) in nitrogen at annealing temperature at 350 °C or above suggest the activation barrier for the equilibrium reaction is around 350 °C. Importantly, it also indicates that the lowest thermal annealing temperature for conversion of akaganeite to magnetite is 350 °C.

Since magnetite is not a photoelectrochemically active material, the magnetite samples were further annealed in air to form hematite, as illustrated in Figure 4.4a. The black N350 sample was annealed on a hot plate at 350 °C in air for 30 min. The black film slowly turned into red color, suggesting formation of hematite. This sample is denoted as NA350. During this air annealing process, a portion of Fe^{2+} sites in magnetite are believed to be re-oxidized back to Fe^{3+} . A control hematite sample was prepared by directly annealing of $\beta\text{-FeOOH}$ at 550 °C in air (denoted as A550) for comparison. XRD spectra collected from NA350 and A550 samples showed two sharp peaks that can be indexed to the (110) and (300) diffraction peaks of hematite (JCPDS 33-0664) (Figure 4.4b). Additionally,

they also exhibited characteristic Raman peaks of hematite (Figure 4.4c). The NA350 sample has broader diffraction peaks than A550 sample, suggesting it has relatively lower crystallinity. This is consistent with the existence of defects (oxygen vacancies) in the structure.³⁷

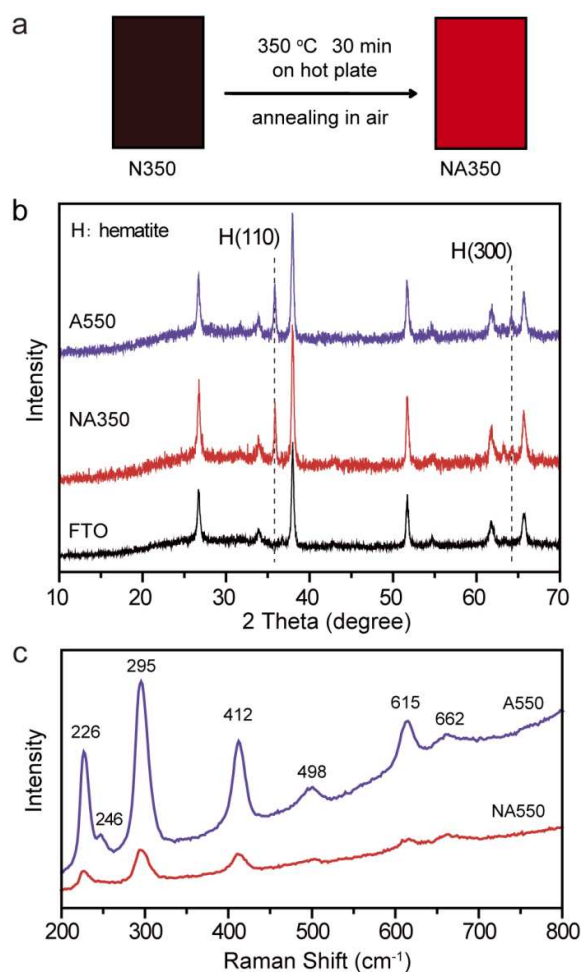


Figure 4.4 (a) A schematic illustration of thermal re-oxidation of magnetite (sample N350) to hematite (sample NA350). (b) XRD spectra collected for NA350, A550 samples, and FTO substrate. Diffraction peaks for hematite (JCPDS 33-0664) are labelled with H(hkl). (c) Raman spectra for NA350 and A550 samples.

To probe the variation of oxidation state of Fe during synthesis and support the presence of Fe^{2+} in NA350 sample, we collected Fe 2p X-ray photoelectron spectroscopy (XPS) spectra for NA350, and A550 samples (Figure 4.5). The Fe $2p_{3/2}$ peaks of both samples are centered at the binding energies of ~ 711.4 eV, which is typical value observed for Fe^{3+} in Fe_2O_3 and Fe_3O_4 .^{5,39,40} Noteworthy that the XPS spectrum for NA350 sample as well as its difference spectrum to A550 sample exhibit an extra satellite peak located at 716.4 eV, which corresponding to Fe^{2+} species.⁴⁰ These results confirm the successfully creation of Fe^{2+} in NA350 sample.

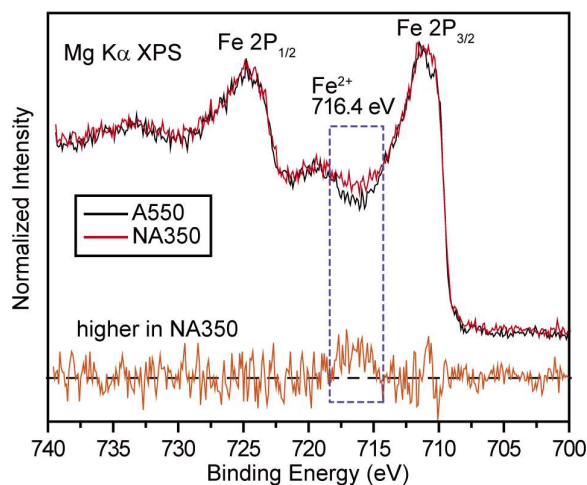


Figure 4.5 Overlay of Fe 2p XPS spectra of A550 (black), and NA350 (red) samples, together with their difference spectra (“NA350” minus “A550”). The vertical dashed lines highlight the satellite peaks for Fe^{3+} and Fe^{2+} species.

Furthermore, electrochemical impedance spectroscopy (EIS) measurements were carried out to reveal the influence of forming oxygen vacancies on the

electronic properties of NA350 and A550 hematite samples. The system was allowed to equilibrate for 5 min. An alternating-current perturbation of the applied potential (0.4V vs Ag/AgCl with a magnitude of 5 mV and frequencies changing from 100 kHz to 1 Hz) was then exerted, and the impedance changes in response to the perturbation were measured.⁴¹ Figure 4.6 shows the Nyquist diagrams collected from NA350 and A550 samples. By fitting the semicircular arcs in the Nyquist plot to an equivalent Randle circuit,¹³ the charge transfer resistances (R_{ct}) for A550 and NA350 samples are calculated to be 104 and 23.1 k Ω , respectively. This result supports our hypothesis that the introduction of oxygen vacancies into hematite at low temperature can improve the charge transfer efficiency. The enhanced charge transfer is believed to be due to the electrical conductivity as a result of formation of oxygen vacancies.

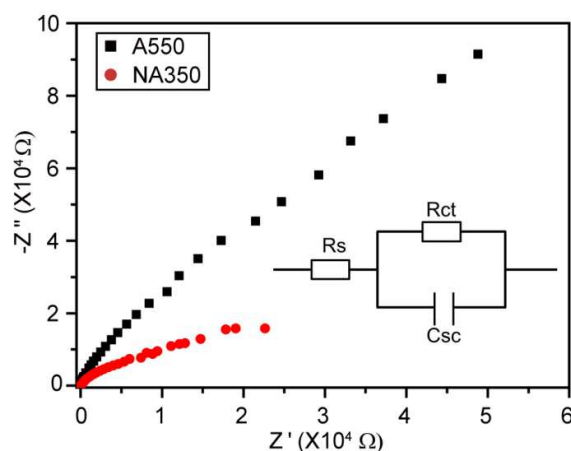


Figure 4.6 Nyquist plots of the impedance of A550 and NA350 collected at 0.4V vs. Ag/AgCl under 1 sun illumination. The frequency varied from 100 kHz to 1 Hz. Z' and Z'' are the real and imaginary parts of the impedance, respectively. Inset: A diagram of the equivalent Randles circuit model used to fit

the impedance data between 1 and 100 kHz. R_s is the solution resistance, C_{sc} is the space charge capacitance, and R_{ct} is the charge transfer resistance across the interface of electrode/electrolyte.

The hematite films (NA350 and A550) were fabricated into photoanode and tested for photoelectrochemical performance in a three electrode system in 1M KOH solution (pH 13.6) under 1 sun illumination, using a Pt counter electrode and a Ag/AgCl (1M KCl) reference electrode. As shown in Figure 6.7, A550 sample yielded a tiny photocurrent density less than $5 \mu\text{A}/\text{cm}^2$ at potential of 0.45 V vs. Ag/AgCl or below. This is consistent with the previous results obtained from hydrothermally grown hematite nanowires.^{6,20,34} High temperature annealing (higher than 650 °C) was required to activate these hematite nanowires for PEC water oxidation.^{6,20,33,34} In contrast, NA350 sample showed pronounced photoactivity in the same potential range we studied, and achieved a photocurrent density of $0.10 \text{ mA}/\text{cm}^2$ at 0.4 V vs. Ag/AgCl. This is the first demonstration of photoactive hematite nanowire obtained at such a low annealing temperature (350 °C).

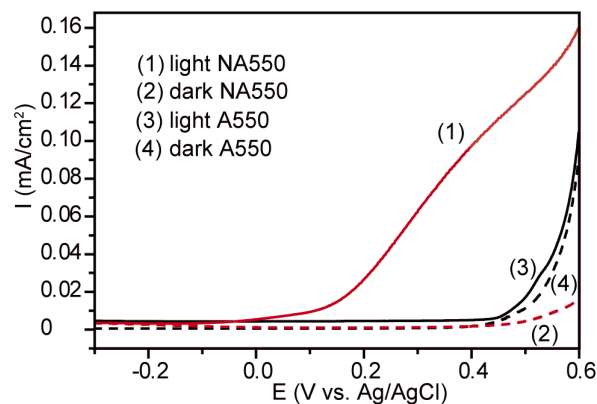


Figure 4.7 Linear sweep voltammograms collected for A550 photoanode and NA350 photoanode, at a scan rate of 10 mV s^{-1} , in a KOH electrolyte solution (1 M , pH 13.6) under illumination by simulated solar light of 100 mW cm^{-2} and in the dark (dashed lines).

Figure 4.8 shows the incident photo-to-current conversion efficiency (IPCE) profiles of NA350 and A550 collected at $0.4 \text{ V vs. Ag/AgCl}$. IPCE values at specific wavelengths were calculated based on the equation reported elsewhere.⁴³ Their IPCE values gradually decrease to zero at around 580 nm , which is consistent with the bandgap of hematite. Importantly, NA350 sample exhibits significantly enhanced IPCE compared to the A550 sample, over the entire wavelength range between 300 and 650 nm . The IPCE data also suggest that the creation of oxygen vacancies did not change the bandgap of hematite, and the enhanced IPCE of NA350 should be attributed to the improved efficiency of charge collection.

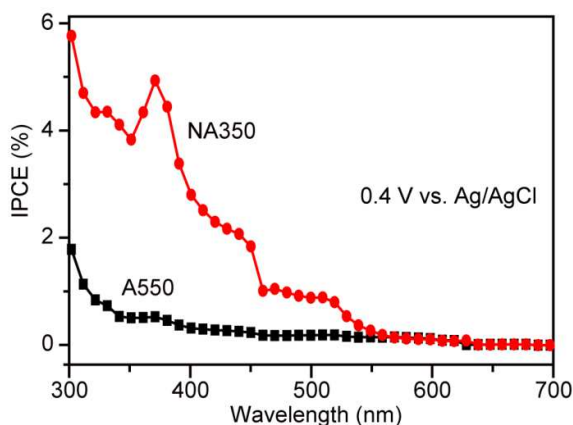


Figure 4.8 IPCE spectra of A550 (square) and NA350 (circle), collected at $0.4 \text{ V vs. Ag/AgCl}$.

In previous studies, element-doped hematite structures have shown noticeably improved PEC performance compared to pristine hematite.^{5,6} We seek to further improve the photoactivity of oxygen-deficient hematite sample by incorporating extrinsic dopants in the growth process. We prepared the Sn-doped FeOOH sample by mixing the Sn precursor (10 mg/mL SnCl₄ ethanol solution) in 0.15M FeCl₃ solution with 1M NaNO₃ (pH 1.5, adjusted by HCl). The as-prepared Sn-doped β -FeOOH film was annealed in pure N₂ at 350 °C for 1 hour, followed by annealing in air at the same temperature for extra 30 minutes. The highest annealing temperature in the entire growth process was still 350 °C. This sample is denoted as Sn-NA350. We also annealed a Sn-doped FeOOH sample directly in air at 550 °C as a control sample, denoted as Sn-A550. The XPS analysis results confirmed the presence of Sn doping in both Sn-550 and Sn-NA350 samples (data not shown). Linear sweep voltammogram shows that the Sn-A550 photoanode exhibits negligible photocurrent (Figure 6.9). In contrast, the Sn-NA350 achieved a significant photocurrent density of 0.35 mA/cm² at 0.4 V vs. Ag/AgCl. This current density is three times higher than that of the undoped sample (NA350) obtained at the same potential.

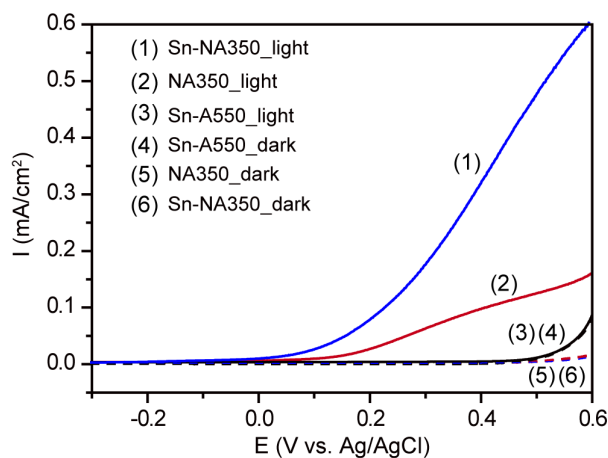


Figure 4.9 Linear sweep voltammograms collected for Sn-A550 photoanode, Sn-NA350 photoanode, and NA350 photoanode at a scan rate of 10 mV s^{-1} , in a NaOH electrolyte solution (1 M, pH 13.6) under illumination (AM1.5G, 100 mW cm^{-2}) and in the dark (dashed lines).

The IPCE also showed an enhancement over the entire wavelength region (300 to 650 nm) (Figure 4.10), which is consistent with the I-V data. Nyquist diagrams were also collected from Sn-NA350, Sn-A550 and NA350 samples to compare the charge transfer kinetics on these working electrodes (Figure 4.11). Charge transfer resistance of Sn-A550 and Sn-NA350 were calculated to be 74.3 and 5.54 $\text{k}\Omega$, confirming the enhanced photoactivity is mainly due to the better charge transfer.

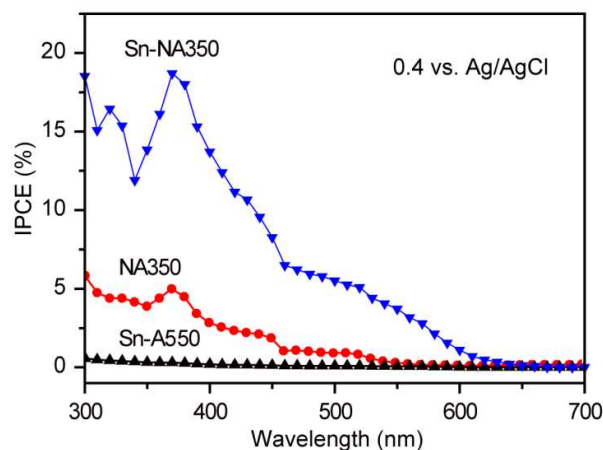


Figure 4.10 IPCE spectra for Sn-A550, Sn-NA350, and NA350 collected at 0.4 V vs. Ag/AgCl.

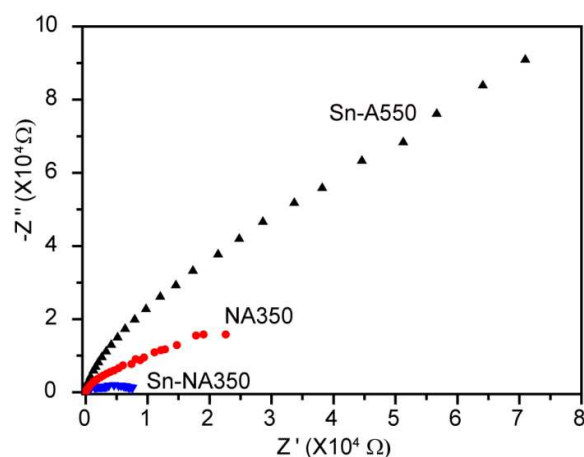


Figure 4.11 Nyquist plots of the impedance of Sn-A550, Sn-NA350 and NA350 collected at 0.4 V vs. Ag/AgCl under illumination. The frequency varied from 100 kHz to 1 Hz.

To investigate the stability of hematite nanowires electrodes prepared by this low temperature annealing method, we measured the photocurrent densities of Sn-NA350 and NA350 samples at 0.4 V vs. Ag/AgCl for 24 hr under illumination (AM 1.5G, 100 mWcm⁻²). As shown in Figure 4.12, both

Sn-NA350 and NA350 samples exhibit stable photocurrent in a KOH electrolyte solution (pH 13.6) for at least one day.

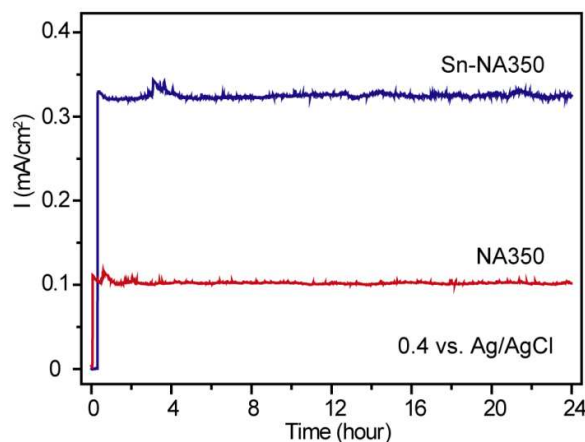


Figure 4.12 Amperometric I-t curve of NA350 and Sn-NA350 measured at 0.4 V vs. Ag/AgCl for 24 hr.

4.4 Conclusion

In conclusion, we have demonstrated that highly photoactive hematite nanowire photoanode can be prepared by a low temperature annealing process. The annealing temperature can be as low as 350 °C, which is the so far lowest activation temperature reported for hematite nanowire photoanode. This temperature is mainly determined by the annealing temperature for creating oxygen vacancies in hematite structure. The formation of oxygen vacancies increase the donor density of hematite, and thus, improved the charge transfer efficiency of the electrode. Significantly, this low temperature annealing approach can also be coupled with Sn doping to further improve the

photoactivity of hematite. Sn-doped hematite nanowires annealed by this two-step process at 350 °C achieved a photocurrent of 0.35 mA/cm² at 0.4 V vs. Ag/AgCl. The capability of activating hematite nanowires at lower temperature is practically important for the fabrication of highly photoactive hematite electrodes.

References

1. Y. Li, J. Z. Zhang, *Laser Photonics Rev.* **2010**, *4*, 517-528.
2. D. A. Wheeler, G. Wang, Y. Ling, Y. Li, J. Z. Zhang, *Energy Environ. Sci.* **2012**, *5*, 6682-6702.
3. B. C. Fitzmorris, J. M. Patete, J. Smith, X. Mascorro, S. Adams, S. S. Wong, J. Z. Zhang, *ChemSusChem* **2013**, DOI: 10.1002/cssc.201300571
4. K. Sivula, F. Le Formal, M. Grätzel, *ChemSusChem* **2011**, *4*, 432-449.
5. G. Wang, Y. Ling, D. A. Wheeler, K. E. N. George, K. Horsley, C. Heske, J. Z. Zhang, Y. Li, *Nano Lett.* **2011**, *11*, 3503-3509.
6. Y. Ling, G. Wang, D. A. Wheeler, J. Z. Zhang, Y. Li, *Nano Lett.* **2011**, *11*, 2119-2125.
7. Y. Ling, G. Wang, J. Reddy, C. Wang, J. Z. Zhang, Y. Li, *Angew. Chem. Int. Ed.* **2012**, *51*, 4074-4079.
8. S. C. Warren, K. Voatchovsky, H. Dotan, C. M. Leroy, M. Cornuz, F.

- Stellacci, C. Habert, A. Rothschild, M. Grätzel, *Nat. Mater.* **2013**, *12*, 842-849.
9. D. Benjelloun, J.-P. Bonnet, J.-P. Doumerc, J.-C. Launay, M. Onillon, P. Hagemuller, *Mater. Chem. Phys.* **1984**, *10*, 503-518.
 10. F. J. Morin, *Physical Review* **1954**, *93*, 1195-1199.
 11. F. J. Morin, *Physical Review* **1951**, *83*, 1005-1010.
 12. A. G. Joly, J. R. Williams, S. A. Chambers, G. Xiong, W. P. Hess, D. M. Laman, *J. Appl. Phys.* **2006**, *99*, 053521.
 13. H. Dotan, K. Sivula, M. Gratzel, A. Rothschild, S. C. Warren, *Energy Environ. Sci.* **2011**, *4*, 958-964.
 14. G. Wang, Y. Ling, X. Lu, T. Zhai, F. Qian, Y. Tong, Y. Li, *Nanoscale* **2013**, *5*, 4129-4133.
 15. Y. Lin, G. Yuan, S. Sheehan, S. Zhou, D. Wang, *Energy Environ. Sci.* **2011**, *4*, 4862-4869.
 16. I. Cesar, K. Sivula, A. Kay, R. Zboril, M. Grätzel, *J. Phys. Chem. C* **2009**, *113*, 772-782.
 17. N. J. Cherepy, D. B. Liston, J. A. Lovejoy, H. M. Deng, J. Z. Zhang, *J. Phys. Chem. B* **1998**, *102*, 770-776.
 18. O. Khaselev, J. A. Turner, *Science* **1998**, *280*, 425-427.
 19. A. Kay, I. Cesar, M. Grätzel, *J. Amer. Chem. Soc.* **2006**, *128*, 15714-15721.
 20. L. Li, Y. Yu, F. Meng, Y. Tan, R. J. Hamers, S. Jin, *Nano Lett.* **2012**, *12*,

724-731.

21. R. van de Krol, Y. Q. Liang, J. Schoonman, *J. Mater. Chem.* **2008**, *18*, 2311-2320.
22. F. Meng, S. A. Morin, S. Jin, *J. Amer. Chem. Soc.* **2011**, *133*, 8408-8411.
23. K. Sun, W. Wei, Y. Jing, Y. Ding, Z. L. Wang, D. Wang, *ChemCommun* **2011**, *47*, 7776 - 7778.
24. P. M. Rao, X. Zheng, *Nano Lett.* **2009**, *9*, 3001-3006.
25. L. Vayssieres, J. H. Guo, J. Nordgren, *Journal of Nanosci. Nanotechnol.* **2001**, *1*, 385-388.
26. L. Vayssieres, N. Beermann, S. E. Lindquist, A. Hagfeldt, *Chem. Mater.* **2001**, *13*, 233-235.
27. R. Franking, L. Li, M. A. Lukowski, F. Meng, Y. Tan, R. J. Hamers, S. Jin, *Energy Environ. Sci.* **2013**, *6*, 500-512.
28. H. Wu, M. Xu, Y. Wang, G. Zheng, *Nano Research* **2013**, *6*, 167-173.
29. J. J. Wu, Y. L. Lee, H. H. Chiang, D. K. P. Wong, *J. Phys. Chem. B* **2006**, *110*, 18108-18111.
30. J. Frydrych, L. Machala, J. Tucek, K. Siskova, J. Filip, J. Pechousek, K. Safarova, M. Vondracek, J. H. Seo, O. Schneeweiss, M. Grätzel, K. Sivula, R. Zboril, *J. Mater. Chem.* **2012**, *22*, 23232-23239.
31. T. Lindgren, H. L. Wang, N. Beermann, L. Vayssieres, A. Hagfeldt, S. E. Lindquist, *Sol. Energy Mater. Sol. Cells* **2002**, *71*, 231-243.

32. L. Xi, S. Y. Chiam, W. F. Mak, P. D. Tran, J. Barber, S. C. J. Loo, L. H. Wong, *Chem. Sci.* **2012**, *4*, 164-169.
33. R. H. Goncalves, B. H. R. Lima, E. R. Leite, *J. Amer. Chem. Soc.* **2011**, *133*, 6012-6019.
34. K. Sivula, R. Zboril, F. Le Formal, R. Robert, A. Weidenkaff, J. Tucek, J. Frydrych, M. Grätzel, *J. Amer. Chem. Soc.* **2010**, *132*, 7436-7444.
35. J. Brillet, M. Grätzel, K. Sivula, *Nano Lett.* **2010**, *10*, 4155-4160.
36. V. M. Aroutiounian, V. M. Arakelyan, G. E. Shahnazaryan, H. R. Hovhannisyan, H. Wang, J. A. Turner, *Solar Energy* **2007**, *81*, 1369-1376.
37. D. L. A. de Faria, S. Venâncio Silva, M. T. de Oliveira, *J. Raman Spectrosc.* **1997**, *28*, 873-878.
38. E. Paterson, R. Swaffield, D. R. Clark, *Thermochim. Acta* **1982**, *54*, 201-211.
39. K. Wandelt, *Surf. Sci. Rep.* **1982**, *2*, 1-121.
40. T. Fujii, F. M. F. de Groot, G. A. Sawatzky, F. C. Voogt, T. Hibma, K. Okada, *Phys. Review B* **1999**, *59*, 3195-3195.
41. Y. Lin, S. Zhou, S. W. Sheehan, D. Wang, *J. Am. Chem. Soc.* **2011**, *133*, 2398-2401.
42. B. Klahr, S. Gimenez, F. Fabregat-Santiago, T. Hamann, J. Bisquert, *J. Am. Chem. Soc.* **2012**, *134*, 4294-4302.
43. Y. C. Pu, G. Wang, K. D. Chang, Y. Ling, Y. K. Lin, R. C. Fitzmorris, C. M.

Liu, X. Lu, Y. Tong, Y. J. Hsu, Y. Li, *Nano Lett.* **2013**, 13, 3817-3823.

Chapter 5

Final Conclusions and Outlook

5.1 Final conclusions of the thesis

The work presented in this thesis aims at improving the photoelectrochemical performance of using hematite as the photoanode for water splitting. In chapter 1, a general introduction and review of basic mechanism of PEC water splitting, the usage of nanostructured hematite, and the photoactivity measurement system in our lab is introduced.

The following three chapters of this thesis focus on modifying the electronic properties of hematite to enhance its PEC performance. The chapter 2 is about unintentional Sn-doping method. As a start and foundation, hematite nanowires were grown on FTO substrate by an aqueous chemical growth method. The as-prepared samples were further annealed in a home-made CVD system at temperature between 550 and 850 °C. Temperature-dependent XPS analysis confirms the incorporation of Sn diffused from FTO substrate into hematite nanowires when the annealing temperature is at or above 650 °C. The Sn atomic ratios (Sn%) of samples increased with sintering temperature. The as-prepared hematite nanowires (sintered at 550 °C) yielded a relatively low photocurrent density of 0.035 mA/cm² at 1.23 V *vs* RHE. Significantly, the

photocurrent densities of these hematite nanowires drastically increased with sintering temperature. The onset temperature was 650 °C, which was consistent with the increase of Sn%. This result suggested a strong correlation between Sn% and photocurrent density of hematite. The sudden drop of photocurrent for the hematite nanowires sintered at 850 °C can be ascribed to the considerably increased resistivity of FTO substrate. The donor densities of hematite can be estimated from the Mott-Schottky plots via electrochemical impedance measurements. The result suggested that donor densities of hematite increased with increased Sn%, from $1.89 \times 10^{19} \text{ cm}^{-3}$ (650 °C) to $5.38 \times 10^{19} \text{ cm}^{-3}$ (800 °C), due to that Sn^{4+} dopant acted as an electronic donor and improves charge transport in hematite nanostructure.

The above work confirms Sn-doping significantly improves the PEC performance of hematite nanostructures by increasing their donor density. However, there are still some issues bothering me. First, high temperature heating and the loss of Sn degrades the electrical conductivity of FTO layer. And, it is certainly not ideal to limit the hematite growth on the FTO substrate. So In chapter 3, an alternative approach, creating oxygen vacancies, has been reported for the enhancement of the carrier density of hematite. The aqueous chemical grown $\beta\text{-FeOOH}$ nanowires were still used as the start substrate. Oxygen vacancies had been introduced into hematite via thermal annealing $\beta\text{-FeOOH}$ in

an oxygen deficient condition at a relatively low temperature (550 °C). The 2P XPS spectra from hematite achieved in such an oxygen deficient condition exhibited obvious satellite peak around 716 eV, which corresponds to Fe²⁺. As we expected, the creation of oxygen vacancies acted as shallow donors and therefore increased the donor density of hematite, which was confirmed by the Mott-Schottky analysis. The mechanism of Fe²⁺ formation was also studied and discussed in that chapter. Based on the control experiments, it was found that the existence of chloride ions in channel of β -FeOOH and the oxygen-deficient atmosphere were essential for creating oxygen vacancies. Over all, highly photoactivated hematite photoanode can be achieved just by a simple change in the thermal decomposition condition of β -FeOOH.

Although these two approaches can give us significantly enhanced PEC performance of hematite, one issue really bothers us is the high activation temperature. It is certainly beneficial if we can lower the activation temperature from practical point of view. In chapter 4, a low temperature activation method is demonstrated. The first step used here was converting β -FeOOH to magnetite (Fe₃O₄) at a low temperature in pure N₂ atmosphere. Therefore, it had a number of oxygen vacancies in magnetite. Temperatures between 200 and 425 °C had been tried. Base on the XRD and Raman spectra, the lowest temperature for the formation of magnetite was around 350 °C. Next step, the achieved magnetite

was converted to hematite at a relatively low temperature (350 °C) in air. In this process, it was expected that some of the oxygen vacancies would be re-oxidized. But certain amount of oxygen vacancies still presented in the hematite, confirmed by XPS spectra. This oxygen deficient hematite appeared a noticeably improved photoactivity. It was the first demonstration of photoactive hematite nanowires obtained at such a low annealing temperature (350 °C). This low temperature annealing approach can also be coupled with Sn doping to further improve the photoactivity of hematite. The capability of activating hematite nanowires at lower temperature is practically important for the fabrication of highly photoactive hematite electrodes.

5.2 Outlook

Although both extrinsic impurities and intrinsic defects have substantially enhanced charge carrier transport in hematite and led to improve the PEC performance of hematite, an outstanding challenge for hematite photoanode is the large onset voltage, due to the slow water oxidation kinetics and low lying conduction band.^{1,2} It still needs a large applied bias typically in the range of 0.8 to 1.0 V *vs.* RHE to obtain photocurrent onset due to the slow water oxidation kinetics.^{1,2} It is critical to reduce the over potential of hematite photoanode. Recent advancement in the development of oxygen evolution reaction (OER) catalysts and heterojunction photoelectrode could potentially address this issue,

and further increase the STH efficiency of hematite photoanodes.^{1, 3-6}

Various OER catalysts such as Co-Pi,⁵⁻⁷ IrO₂,^{8, 9} and NiO_x¹⁰ have been used to modify hematite photoanodes. For example, Zhong *et al.* reported Co-Pi catalyst modified hematite photoanode for PEC water oxidation.⁵⁻⁷ The Co-Pi catalyst was deposited on the surface of hematite film via electrochemical deposition method, by which the thickness of Co-Pi catalyst layer could be easily controlled. The presence of Co-Pi catalyst reduced the onset potential for PEC water oxidation by >350 mV. Therefore, the photocurrent density of Co-Pi modified hematite was significantly enhanced in the lower applied potentials.⁷ These results proved that OER catalyst modification could suppress the water oxidation overpotential of hematite.

The formation of heterojunctions can enable new and/or enhanced function of semiconductor photoelectrodes. Various heterojunction photoelectrode structures such as Si/Fe₂O₃,¹¹ WO₃/Fe₂O₃,¹² and Fe₂O₃/BiVO₄¹³ have shown enhanced performance for PEC hydrogen generation. For example, Mayer and co-workers have reported a hematite/Si nanowires heterostructure as photoanode.¹¹ In this structure, hematite and Si can be independently excited by photons in the solar spectrum having different energies, working as a dual-absorber system. A cathodic shift in the photocurrent onset potential was observed, as a result of enhanced photopotentials developed within these two

materials contributing to enhanced water splitting performance. This device achieved the lowest onset potential (0.6 V vs. RHE) for hematite photoanode without the use of surface catalysts or elemental doping. This results points out a promising direction for improving the efficiency of hematite by using heterojunction to enhance the photovoltages attainable by a single photoanode device and to utilize the solar energy more efficiently.

References

1. Klahr, B.; Gimenez, S.; Fabregat-Santiago, F.; Hamann, T.; Bisquert, J. *J Am Chem Soc* **2012**, 134, (9), 4294-4302.
2. Sivula, K.; Le Formal, F.; Grätzel, M. *ChemSusChem* **2011**, 4, (4), 432-449.
3. Le Formal, F.; Tetreault, N.; Cornuz, M.; Moehl, T.; Gratzel, M.; Sivula, K. *Chemical Science* **2011**, 2, (4), 737-743.
4. Kronawitter, C. X.; Zegkinoglou, I.; Rogero, C.; Guo, J. H.; Mao, S. S.; Himpfel, F. J.; Vayssieres, L. *The Journal of Physical Chemistry C* **2012**, 116, (43), 22780-22785.
5. Zhong, D. K.; Gamelin, D. R. *J Am Chem Soc* **2010**, 132, (12), 4202-4207.
6. Zhong, D. K.; Cornuz, M.; Sivula, K.; Gratzel, M.; Gamelin, D. R. *Energy Environ. Sci.* **2011**, 4, (5), 1759-1764.
7. Zhong, D. K.; Sun, J. W.; Inumaru, H.; Gamelin, D. R. *J Am Chem Soc*

- 2009**, 131, (17), 6086-+.
8. Tilley, S. D.; Cornuz, M.; Sivula, K.; Gratzel, M. *Angew Chem Int Edit* **2010**, 49, (36), 6405-6408.
 9. Badia-Bou, L.; Mas-Marza, E.; Rodenas, P.; Barea, E. M.; Fabregat-Santiago, F.; Gimenez, S.; Peris, E.; Bisquert, J. *The Journal of Physical Chemistry C* **2013**, 117, (8), 3826-3833.
 10. Wang, G.; Ling, Y.; Lu, X.; Zhai, T.; Qian, F.; Tong, Y.; Li, Y. *Nanoscale* **2013**, 5, (10), 4129-4133.
 11. Mayer, M. T.; Du, C.; Wang, D. *J Am Chem Soc* **2012**, 134, (30), 12406-12409.
 12. Sivula, K.; Le Formal, F.; Gratzel, M. *Chem Mater* **2009**, 21, (13), 2862-2867.
 13. Hou, Y.; Zuo, F.; Dagg, A.; Feng, P. *Nano Lett* **2012**, 12, (12), 6464-6473.

Bibliography

- Abdi, F. F.; Han, L.; Smets, A. H. M.; Zeman, M.; Dam, B.; van de Krol, R. *Nat. Commun.* **2013**, 4, 2195.
- Abdi, F. F.; van de Krol, R. *J. Phys. Chem. C* **2012**, 116, (17), 9398-9404.
- Aharon-Shalom, E.; Heller, A. *J. Electrochem. Soc.* **1982**, 129, (12), 2865-2866.
- Aroutiounian, V. M.; Arakelyan, V. M.; Shahnazaryan, G. E.; Hovhannisyanyan, H. R.; Wang, H.; Turner, J. A. *SoEn* **2007**, 81, (11), 1369-1376.
- Bak, T.; Nowotny, J.; Rekas, M.; Sorrell, C. C. *Int. J. Hydrogen Energ.* **2002**, 27, (10), 991-1022.
- Bjorksten, U.; Moser, J.; Gratzel, M. *Chem Mater* **1994**, 6, (6), 858-863.
- Boettcher, S. W.; Warren, E. L.; Putnam, M. C.; Santori, E. A.; Turner-Evans, D.; Kelzenberg, M. D.; Walter, M. G.; McKone, J. R.; Brunschwig, B. S.; Atwater, H. A.; Lewis, N. S. *J Am. Chem. Soc.* **2011**, 133, (5), 1216-1219.
- Brillet, J.; Grätzel, M.; Sivula, K. *Nano Lett.* **2010**, 10, (10), 4155-4160.
- Cao, Y.; He, T.; Zhao, L.; Wang, E.; Yang, W.; Cao, Y. *J. Phys. Chem. C* **2009**, 113, 18121-18123.
- Cesar, I.; Kay, A.; Martinez, J. A. G.; Grätzel, M. *J. Am. Chem. Soc.* **2006**, 128, (14), 4582-4583.
- Cesar, I.; Sivula, K.; Kay, A.; Zboril, R.; Grätzel, M. *J. Phys. Chem. C* **2009**, 113, (2), 772-782.

Cherepy, N. J.; Liston, D. B.; Lovejoy, J. A.; Deng, H. M.; Zhang, J. Z. *J Phys Chem B* **1998**, 102, (5), 770-776.

Cooper, J. K.; Ling, Y.; Longo, C.; Li, Y.; Zhang, J. Z. *J. Phys. Chem. C* **2012**, 116, (33), 17360-17368.

Coridan, R. H.; Shaner, M.; Wiggernhorn, C.; Brunschwig, B. S.; Lewis, N. S. *J. Phys. Chem. C* **2013**, 117, (14), 6949-6957.

Cristino, V.; Caramori, S.; Argazzi, R.; Meda, L.; Marra, G. L.; Bignozzi, C. A. *Langmuir* **2011**, 27, (11), 7276-7284.

Dareedwards, M. P.; Goodenough, J. B.; Hamnett, A.; Trelvellick, P. R. *Chem. Soc., Faraday Trans. I* **1983**, 79, 2027-2041.

DeSario, P. A.; Pietron, J. J.; DeVantier, D. E.; Brintlinger, T. H.; Stroud, R. M.; Rolison, D. R. *Nanoscale* **2013**, 5, (17), 8073-8083.

Esposito, D. V.; Forest, R. V.; Chang, Y.; Gaillard, N.; McCandless, B. E.; Hou, S.; Lee, K. H.; Birkmire, R. W.; Chen, J. G. *Energy Environ. Sci.* **2012**, 5, (10), 9091-9099.

Feng X.; Shankar K.; Varghese O. K.; Paulose M.; Latempa T. J.; Grimes C. A.; *Nano Lett.* **2008**, 8, 3781.

Franking, R.; Li, L.; Lukowski, M. A.; Meng, F.; Tan, Y.; Hamers, R. J.; Jin, S. *Energy Environ. Sci.* **2013**, 6, (2), 500-512.

Frites, M.; Shaban, Y. A.; Khan, S. U. M. *Int. J. Hydrogen Energy* **2010**, 35, (10), 4944-4948.

Fujishima, A.; Honda, K. *Nature* **1972**, 238, (5358), 37-38.

Gaudon, M.; Pailhe, N.; Majimel, J.; Wattiaux, A.; Abel, J.; Demourgues, A. *J. Solid State Chem.* **2010**, 183, (9), 2101-2109.

Glasscock, J. A.; Barnes, P. R. F.; Plumb, I. C.; Savvides, N. *J. Phys. Chem. C* **2007**, 111, (44), 16477-16488.

Goncalves, R. H.; Lima, B. H. R.; Leite, E. R. *J. Am. Chem. Soc.* **2011**, 133, (15), 6012-6019.

Grätzel, M. *Nature* **2001**, 414, (6861), 338-344.

Grätzel, M.; Kiwi, J.; Morrison, C. L.; Davidson, R. S.; Tseung, A. C. C. *J. Chem. Soc., Faraday Trans. I* **1985**, 81, 1883-1890.

Hahn, N. T.; Mullins, C. B. *Chem. Mater.* **2010**, 22, (23), 6474-6482.

Hensel, J.; Wang, G.; Li, Y.; Zhang, J. Z. *Nano Lett.* **2010**, 10, 478-483.

Heller, A. *Science* **1984**, 223, (4641), 1141-1148.

Hoang, S.; Guo, S.; Hahn, N. T.; Bard, A. J.; Mullins, C. B. *Nano Lett.* **2012**, 12, (1), 26-32.

Hoang, S.; Berglund, S. P.; Hahn, N. T.; Bard, A. J.; Mullins, C. B. *J. Am. Chem. Soc.* **2012**, 134, (8), 3659-3662.

Hu, Y. S.; Kleiman-Shwarsstein, A.; Forman, A. J.; Hazen, D.; Park, J. N.; McFarland, E. W. *Chem. Mater.* **2008**, 20, (12), 3803-3805.

Hwang, Y. J.; Hahn, C.; Liu, B.; Yang, P. *ACS Nano* **2012**, 6, (6), 5060-5069.

Inglér, W. B.; Khan, S. U. M. *Thin Solid Films* **2004**, 461, (2), 301-308.

Ingler, W. B.; Khan, S. U. M. *Electrochem. Solid-State Lett.* **2006**, 9, (4), G144-G146.

Iordanova, N.; Dupuis, M.; Rosso, K. M. *J. Chem. Phys.* **2005**, 122, 144305.

Iwase, A.; Kudo, A. *J. Mater. Chem.* **2010**, 20, (35), 7536-7542.

Joly, A. G.; Williams, J. R.; Chambers, S. A.; Xiong, G.; Hess, W. P.; Laman, D. *M. J. Appl. Phys.* **2006**, 99, 053521

Jang, J. S.; Lee, J.; Ye, H.; Fan, F. R. F.; Bard, A. J. *J. Phys. Chem. C* **2009**, 113, (16), 6719-6724.

Jang, J. S.; Yoon, K. Y.; Xiao, X.; Fan, F.-R. F.; Bard, A. J. *Chem Mater* **2009**, 21, (20), 4803-4810.

Jin, T.; Diao, P.; Wu, Q.; Xu, D.; Hu, D.; Xie, Y.; Zhang, M. *Applied Catalysis B:*

Park, H. S.; Lee, H. C.; Leonard, K. C.; Liu, G.; Bard, A. J. *Chemphyschem* **2013**, 14, (10), 2277-2287.

Kay, A.; Cesar, I.; Grätzel, M. *J. Am. Chem. Soc.* **2006**, 128, (49), 15714-15721.

Kennedy, J. H.; Anderman, M.; Shinar, R. *J Electrochem Soc* **1981**, 128, (11), 2371-2373.

Kleiman-Shwarsstein, A.; Hu, Y. S.; Forman, A. J.; Stucky, G. D.; McFarland, E. *W. J. Phys. Chem. C* **2008**, 112, (40), 15900-15907.

Kumari, S.; Singh, A. P.; Sonal; Deva, D.; Shrivastav, R.; Dass, S.; Satsangi, V. *R. Int. J. Hydrogen Energ.* **2010**, 35, (9), 3985-3990.

Klahr, B.; Gimenez, S.; Fabregat-Santiago, F.; Hamann, T.; Bisquert, J. *J Am Chem Soc* **2012**, 134, (9), 4294-4302.

Kronawitter, C. X.; Vayssieres, L.; Shen, S.; Guo, L.; Wheeler, D. A.; Zhang, J. Z.; Antoun, B. R.; Mao, S. S. *Energy Environ. Sci.* **2011**, 4, (10), 3889-3899.

Le Formal, F.; Grätzel, M.; Sivula, K. *Adv. Funct. Mater.* **2010**, 20, (7), 1099-1107.

Li, L.; Yu, Y.; Meng, F.; Tan, Y.; Hamers, R. J.; Jin, S. *Nano Lett* **2012**, 12, (2), 724-731.

Li, Y.; Zhang, J. Z. *Laser & Photonics Rev.* **2010**, 4, (4), 517-528.

Liang, Y.; Tsubota, T.; Mooij, L. P. A.; van de Krol, R. *J. Phys. Chem. C* **2011**, 115, (35), 17594-17598.

Liang, Y. Q.; Enache, C. S.; van de Krol, R. *Int. J. Photoenergy* **2008**, 739864.

Lin, Y.-G.; Hsu, Y.-K.; Chen, Y.-C.; Chen, L.-C.; Chen, S.-Y.; Chen, K.-H. *Nanoscale* **2012**, 4, (20), 6515-6519.

Lin, Y.; Yuan, G.; Sheehan, S.; Zhou, S.; Wang, D. *Energy Environ. Sci.* **2011**, 4, (12), 4862-4869.

Lin, Y.; Zhou, S.; Sheehan, S. W.; Wang, D. *J. Am. Chem. Soc.* **2011**, 133, 2398-2401.

Lin, Y.; Zhou, S.; Liu, X. H.; Sheehan, S. W.; Wang, D. *J. Am. Chem. Soc.*, **2009**, 131, 2772-2773.

Lin, Y.; S., Z.; Sheehan, S. W.; Wang, D. *J. Am. Chem. Soc.* **2011**, 133, 2398-2401.

Lindgren, T.; Wang, H.; Beermann, N.; Vayssieres, L.; Hagfeldt, A.; Lindquist, S.

Sol. Energy Mater. Sol. Cells **2002**, 71, 231–243.

Ling, Y.; Wang, G.; Reddy, J.; Wang, C.; Zhang, J. Z.; Li, Y. *Angew. Chem.* **2012**, 124, (17), 4150-4155.

Ling, Y.; Wang, G.; Wheeler, D. A.; Zhang, J. Z.; Li, Y. *Nano Lett.* **2011**, 11, (5), 2119-2125.

Liu, C.; Tang, J.; Chen, H. M.; Liu, B.; Yang, P. *Nano Lett.* **2013**, 13, (6), 2989-2992.

Liu, J.; Liang, C.; Zhang, H.; Tian, Z.; Zhang, S. *J. Phys. Chem. C* **2012**, 116, (8), 4986-4992.

Liu, R.; Lin, Y.; Chou, L. Y.; Sheehan, S. W.; He, W.; Zhang, F.; Hou, H. J. M.; Wang D. *Angew. Chem. Int. Ed.*, **2011**, 50, 499-502.

Liang, Y. Q.; Enache, C. S.; van de Krol, R. *Int J Photoenergy* **2008**.

Morrish, R.; Rahman, M.; MacElroy, J. M. D.; Wolden, C. A. *ChemSusChem* **2011**, 4, (4), 474-479.

Newhouse, R.; Wang, H.; Hensel, J.; Wheeler, D.; Zou, S.; Zhang, J. Z. *J. Phys. Chem. Lett.* **2011**, 2, 228-235.

Ni, M.; Leung, M. K. H.; Leung, D. Y. C.; Sumathy, K. *Renew. Sust. Energy Rev.* **2007**, 11, (3), 401-425.

Pu, A.; Deng, J.; Li, M.; Gao, J.; Zhang, H.; Hao, Y.; Zhong, J.; Sun, X. *J. Mater. Chem. A* **2014**, 2, (8), 2491-2497.

Pu, Y.-C.; Wang, G.; Chang, K.-D.; Ling, Y.; Lin, Y.-K.; Fitzmorris, B. C.; Liu,

C.-M.; Lu, X.; Tong, Y.; Zhang, J. Z.; Hsu, Y.-J.; Li, Y. *Nano Lett.* **2013**, 13, (8), 3817-3823.

Sartoretti, C. J.; Alexander, B. D.; Solarska, R.; Rutkowska, W. A.; Augustynski, J.; Cerny, R. *J. Phys. Chem. B* **2005**, 109, (28), 13685-13692.

Satsangi, V. R.; Kumari, S.; Singh, A. P.; Shrivastav, R.; Dass, S. *Int J Hydrogen Energ.* **2008**, 33, (1), 312-318.

Sayama, K.; Nomura, A.; Arai, T.; Sugita, T.; Abe, R.; Yanagida, M.; Oi, T.; Iwasaki, Y.; Abe, Y.; Sugihara, H. *J. Phys. Chem. B* **2006**, 110, (23), 11352-11360.

Shen, S.; Kronawitter, C. X.; Wheeler, D. A.; Guo, P.; Lindley, S. A.; Jiang, J.; Zhang, J. Z.; Guo, L.; Mao, S. S. *J. Mater. Chem. A* **2013**, 1, (46), 14498-14506.

Shi, J.; Starr, M. B.; Xiang, H.; Hara, Y.; Anderson, M. A.; Seo, J.-H.; Ma, Z.; Wang, X. *Nano Lett.* **2011**, 11, (12), 5587-5593.

Sivula, K. *J. Phys. Chem. Lett.* **2013**, 4, (10), 1624-1633.

Sivula, K.; Le Formal, F.; Grätzel, M. *ChemSusChem* **2011**, 4, (4), 432-449.

Sivula, K.; Le Formal, F.; Grätzel, M. *Chem. Mater.* **2009**, 21, (13), 2862-2867.

Sivula, K.; Zboril, R.; Le Formal, F.; Robert, R.; Weidenkaff, A.; Tucek, J.; Frydrych, J.; Gratzel, M. *J. Am. Chem. Soc.* **2010**, 132, (21), 7436-7444.

Solarska R.; Krolikowska A.; Augustynski J.; *Angew. Chem. Int. Ed.* **2011**, 49, 7980.

Su, J. Z.; Guo, L. J.; Bao, N. Z.; Grimes, C. A. *Nano Lett.* **2011**, 11, (5),

1928-1933.

Su, J.; Guo, L.; Bao, N.; Grimes, C. A. *Nano Lett.* **2011**, 11, (5), 1928-1933.

Su, J.; Guo, L.; Yoriya, S.; Grimes, C. A. *Cryst. Growth Des.* **2009**, 10, (2), 856-861.

Tilley, S. D.; Cornuz, M.; Sivula, K.; Grätzel, M. *Angew. Chem. Int. Ed.* **2010**, 49, (36), 6405-6408.

Uchiyama, H.; Yukizawa, M.; Kozuka, H. *J. Phys Chem C* **2011**, 115, (14), 7050-7055.

Vayssieres, L.; Beermann, N.; Lindquist, S. E.; Hagfeldt, A. *Chem. Mater.* **2001**, 13, (2), 233-235.

Vayssieres, L.; Guo, J. H.; Nordgren, J. *J. Nanosci. Nanotechnol.* **2001**, 1, (4), 385-388.

Vayssieres, L.; Sathe, C.; Butorin, S. M.; Shuh, D. K.; Nordgren, J.; Guo, J. H. *Adv Mater* **2005**, 17, (19), 2320-2323.

Walter, M. G.; Warren, E. L.; McKone, J. R.; Boettcher, S. W.; Mi, Q. X.; Santori, E. A.; Lewis, N. S.; *Chem. Rev.* **2010**, 110, 6446.

Wang, H.; Wang, G.; Ling, Y.; Lepert, M.; Wang, C.; Zhang, J. Z.; Li, Y. *Nanoscale* **2012**, 4, (5), 1463-1466.

Wang, H. L.; Turner, J. A. *J. Electrochem. Soc.* **2010**, 157, (11), F173-F178.

Wang, G.; Ling, Y.; Li, Y. *Nanoscale* **2012**, 4, (21), 6682-6691.

Wang, G.; Ling, Y.; Lu, X.; Qian, F.; Tong, Y.; Zhang, J. Z.; Lordi, V.; Rocha

- Leao, C.; Li, Y. *J. Phys. Chem. C* **2013**, 117, (21), 10957-10964.
- Wang, G.; Ling, Y.; Wang, H.; Xihong, L.; Li, Y. *J. Photochem. Photobio. C: Photochem. Rev.* **2014**, 19, (0), 35-51.
- Wang, G.; Ling, Y.; Wang, H.; Yang, X.; Wang, C.; Zhang, J. Z.; Li, Y. *Energy Environ. Sci.* **2012**, 5, (3), 6180-6187.
- Wang, G.; Ling, Y.; Wheeler, D. A.; George, K. E. N.; Horsley, K.; Heske, C.; Zhang, J. Z.; Li, Y. *Nano Lett.* **2011**, 11, (8), 3503-3509.
- Wang, G.; Wang, H.; Ling, Y.; Tang, Y.; Yang, X.; Fitzmorris, R. C.; Wang, C.; Zhang, J. Z.; Li, Y. *Nano Lett.* **2011**, 11, (7), 3026-3033.
- Wang, G. M.; Yang, X. Y.; Qian, F.; Zhang, J. Z.; Li, Y. *Nano Lett.* **2010**, 10, (3), 1088-1092.
- Warren, E. L.; Boettcher, S. W.; McKone, J. R.; Lewis, N. S. In *Photoelectrochemical water splitting: silicon photocathodes for hydrogen evolution*, 2010; pp 77701F-77701F-7.
- Warren, S. C.; Voatchovsky, K.; Dotan, H.; Leroy, C. M.; Cornuz, M.; Stellacci, F.; Habert, C.; Rothschild, A.; Gratzel, M. *Nat. Mater.* **2013**, 12, (9), 842-849.
- Wheeler, D. A.; Wang, G.; Ling, Y.; Li, Y.; Zhang, J. Z. *Energy Environ. Sci.* **2012**, 5, (5), 6682-6702.
- Xi, L.; Chiam, S. Y.; Mak, W. F.; Tran, P. D.; Barber, J.; Loo, S. C. J.; Wong, L. H. *Chemical Science* **2012**.
- Xie, S.; Lu, X.; Zhai, T.; Li, W.; Yu, M.; Liang, C.; Tong, Y. *J Mater Chem* **2012**,

22, (28), 14272-14275.

Xie, S.; Lu, X.; Tong, Y. In *An effective way to enhance photoelectrochemical photoactivity and stability of ZnO nanorod arrays by carbon and nitrogen co-treatment*, International Photonics and Optoelectronics Meetings (POEM), Wuhan, 2013; Optical Society of America: Wuhan, 2013; p ASa3A.28.

Xu, M.; Da, P.; Wu, H.; Zhao, D.; Zheng, G. *Nano Lett.* **2012**, 12, (3), 1503-1508.

Yang, X. Y.; Wolcott, A.; Wang, G. M.; Sobo, A.; Fitzmorris, R. C.; Qian, F.; Zhang, J. Z.; Li, Y. *Nano Lett.* **2009**, 9, (6), 2331-2336.

Ye, H.; Lee, J.; Jang, J. S.; Bard, A. J. *The Journal of Physical Chemistry C* **2010**, 114, (31), 13322-13328.

Zhang, J. Z. *J. Phys. Chem. B* **2000**, 104, 7239-7253.

Zhang, M.; Luo, W.; Li, Z.; Yu, T.; Zou, Z. *Appl. Phys. Lett.* **2010**, 97, 042105.

Zhang, X.; Lu, X.; Shen, Y.; Han, J.; Yuan, L.; Gong, L.; Xu, Z.; Bai, X.; Wei, M.; Tong, Y.; Gao, Y.; Chen, J.; Zhou, J.; Wang, Z. L. *Chem. Commun. (Camb.)* **2011**, 47, (20), 5804-5806.

Environmental **2014**, 148-149, 304-310.

Zhen, C.; Wang, L.; Liu, L.; Liu, G.; Lu, G. Q.; Cheng, H.-M. *Chem. Commun. (Camb.)* **2013**, 49, (55), 6191-6193.

Zhong, D. K.; Choi, S.; Gamelin, D. R. *J. Am. Chem. Soc.* **2011**, 133, (45), 18370-18377.

Zhong, D. K.; Sun, J. W.; Inumaru, H.; Gamelin, D. R. *J. Am. Chem. Soc.* **2009**, 131, (17), 6086-6087.

Zhou, M.; Wu, H. B.; Bao, J.; Liang, L.; Lou, X. W.; Xie, Y. *Angew. Chem. Int. Ed.* **2013**, 52, (33), 8579-8583.